nature communications

Article

https://doi.org/10.1038/s41467-024-51469-5

Unusual plastic strain-induced phase transformation phenomena in silicon

Received: 23 March 2024

Accepted: 7 August 2024

Published online: 15 August 2024

Check for updates

Sorb Yesudhas[1] ✉, Valery I. Levitas[1,2,3] ✉, Feng Lin[1], K. K. Pandey[4] & Jesse S. Smith[5]

Pressure-induced phase transformations (PTs) in Si, the most important electronic material, have been broadly studied, whereas strain-induced PTs have never been studied in situ. Here, we reveal in situ various important plastic strain-induced PT phenomena. A correlation between the direct and inverse Hall-Petch effect of particle size on yield strength and pressure for strain-induced PT is predicted theoretically and confirmed experimentally for Si-I→Si-II PT. For 100 nm particles, the strain-induced PT Si-I→Si-II initiates at 0.3 GPa under both compression and shear while it starts at 16.2 GPa under hydrostatic conditions. The Si-I→Si-III PT starts at 0.6 GPa but does not occur under hydrostatic pressure. Pressure in small Si-II and Si-III regions of micron and 100 nm particles is ~5–7 GPa higher than in Si-I. For 100 nm Si, a sequence of Si-I → I + II → I + II + III PT is observed, and the coexistence of four phases, Si-I, II, III, and XI, is found under torsion. Retaining Si-II and single-phase Si-III at ambient pressure and obtaining reverse Si-II→Si-I PT demonstrates the possibilities of manipulating different synthetic paths. The obtained results corroborate the elaborated dislocation pileup-based mechanism and have numerous applications for developing economic defect-induced synthesis of nanostructured materials, surface treatment (polishing, turning, etc.), and friction.

Silicon is the most important semiconducting element due to its extensive applications in microelectronics, integrated circuits, photovoltaics, micro, and nano-electromechanical systems (MEMS/NEMS) technologies, etc[1,2]. Polycrystalline Si is widely used in solar panels, thin transistors, and large-scale integration manufacturing[3]. When the Si crystals or grains are scaled down to nanometer size, they show remarkable electronic, mechanical, thermoelectric, and optical properties[4–8]. Si possesses numerous high-pressure polymorphs, seven of which (Fig. 1) will be studied here under slow compression/torsion/decompression at room temperature. In addition to the ambient semiconducting Si-I phase, the other metastable Si-III, Si-IV, and Si-XII phases are promising candidates for engineering applications owing to their interesting electronic and optical properties. However, their synthesis requires high pressure/temperature, especially in single-phase form. Recently, single-phase Si-III was synthesized from Si-I at 14 GPa and ~900 K and quenching over 3 days or through a chemical pathway in a Na-Si mixture at 9.5 GPa and ~1000 K[9]. Similar studies reveal that Si-III is an ultranarrow band gap semiconductor (band gap, E_g ~30 eV) with much lower thermal conductivity compared with Si-I and is found to have the potential for infrared plasmonic applications[10]. Si-IV can be obtained from Si-III by annealing. High-pressure torsion (i.e., large plastic shear under pressure) processing of Si at 24 GPa and 10 anvil rotations was used to obtain nanostructured metastable Si-III and Si-XII phases[11,12]. These pressures are too high for

[1]Department of Aerospace Engineering, Iowa State University, Ames, Iowa, USA. [2]Department of Mechanical Engineering, Iowa State University, Ames, Iowa, USA. [3]Ames National Laboratory, Iowa State University, Ames, Iowa, USA. [4]High Pressure & Synchrotron Radiation Physics Division, Bhabha Atomic Research Centre, Mumbai, India. [5]HPCAT, X-ray Science Division, Argonne National Laboratory, Argonne, Lemont, Illinois, USA. ✉e-mail: sorbya@iastate.edu; vlevitas@iastate.edu

https://doi.org/10.1038/s41467-024-51469-5

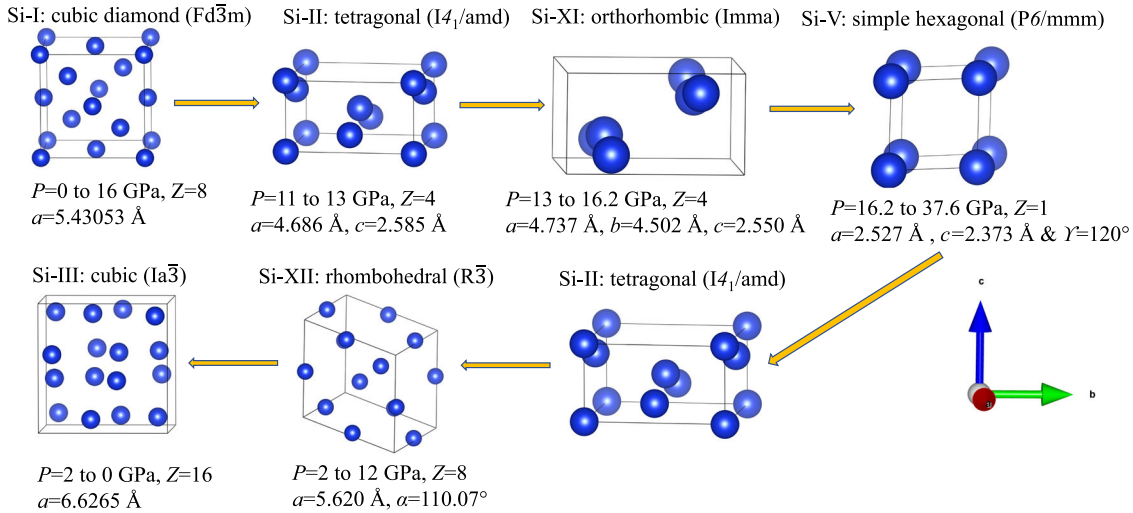

Fig. 1 | Silicon phases obtained during hydrostatic loading and slow unloading for bulk Si [14,17]. Designations, types of lattices, and symmetry groups are shown on the top. The pressure range of stability of phases, number of atoms per formula unit (Z), and lattice parameters are given at the bottom.

industrial applications; we will show that we can drastically reduce them by plastic straining of nanograined Si-I.

The in situ hydrostatic[13–17], uniaxial[7,18–20], and indentation studies of Si[17,21,22], including nanoindentation, nanospheres, and micropillars under compression-decompression, are very extensive. However, many processes – like friction, machining, dicing, lapping, scribing, and polishing of Si wafers and polycrystals, and producing nanostructured Si phases are accompanied by large plastic shear, which may strongly alter the PT pressures[23–28]. As formulated in[23], there is a fundamental difference between PTs under hydrostatic and non-hydrostatic compression below the yield (pressure- and stress-induced PTs) and PTs during plastic flow (strain-induced PTs). The pressure-induced PTs are initiated by nucleation at the pre-existing defects, like dislocations or grain boundaries, which produce a concentration of all stress tensor components. In contrast, plastic strain-induced PTs occur at new defects constantly generated during the plastic flow. Plastic strain-induced PTs may occur at much lower pressure, follow strain-controlled (instead of time-controlled) kinetics, and provide avenues to explore hidden phases, which cannot be obtained under hydrostatic compression[23–28]. The plastic strain-induced PTs require completely different experimental characterization and thermodynamic and kinetic descriptions. The suggested mechanism for a strong reduction of the PT pressure is based on the barrierless nucleation at the dislocation pileups[23], i.e., the dislocation pileup-based mechanism (DPBM). Indeed, the concentration of all stress components is proportional to the number of dislocations N in a pileup[29]; since N can be large, from 10 to 100, local stresses may also be very large. However, as we will show below, this model predicts the wrong grain size dependence of the minimum PT pressure. The entire field of strain-induced PT under high pressure is still in its infancy, with the only in situ study for α-ω PT in Zr[28].

While there are hundreds of publications on PTs in Si under quasi-hydrostatic conditions in a diamond anvil cell (DAC) and nanoindentation, only one quite old work on PTs under compression and shear in rotational DAC (RDAC)[24,30], utilizing only optical and electric resistivity measurements, without in situ x-ray diffraction (XRD), wherein the authors claim a PT sequence, Si-I→III→II. Later[31], a TEM study found that Si-I→IV→III PT occurs at 2–4 GPa, while Si-I→III→II occurs at higher pressures. These claims contradict our in situ synchrotron XRD results in Table 1. Also, it is known that particle/grain size reduction increases the PT pressure for pressure-induced PTs[32]; however, there are no similar studies for strain-induced PTs for any material. The fundamental problem for Si (and any other material) is: what is the PT behavior of Si under severe plastic deformations? Is it possible to drastically reduce the PT pressure, manipulate PT pathways, retain desired phases, find some rules/correlations, and shed light on possible physical mechanisms?

Here, we present in situ synchrotron XRD studies of various plastic strain-induced PTs in Si with three different particle sizes, ~1 μm, 100 nm, and 30 nm, compared with pressure-induced PTs, and reveal several unexpected phenomena and transformation paths. Based on the elaborated DPBM, we predicted with a simple qualitative analytical model and confirmed for Si-I→Si-II PT correlation between the observed particle/crystallite size dependence of the minimum pressure for strain-induced PT and the grain size's direct and inverse Hall–Petch effect on the yield strength. For 100 nm and micron Si, pressure in small Si-II regions is ~5–7 GPa higher than in Si-I, while for pressure-induced PT, it is 2.7 GPa lower due to a 22% volume reduction. For 30 nm Si, the increase is 1.6 GPa only, consistent with reduced dislocation activity in the region of the inverse Hall–Petch effect and increased PT pressure. All these strongly support stress concentration due to DPBM. For 100 nm Si, the minimum pressure for strain-induced PT Si-I→Si-II is p_ε^d = 0.3 GPa, 54 times lower than p_h^d = 16.2 GPa under hydrostatic conditions and 35 times below the phase equilibrium pressure. It is found to be the same for compression in DAC and torsion in RDAC, i.e., it is independent of the plastic strain tensor and its path, which is an unexpected fundamental result. It allows studying strain-induced PTs not only in RDAC, i.e., just by a few dozen groups worldwide, but also in ordinary DAC, i.e., in each high-pressure laboratory. The strain-induced PT Si-I→Si-III initiates at 0.6 GPa for 100 nm Si, and PT Si-I→Si-II starts at 4.9 GPa for 30 nm Si, but both do not occur under hydrostatic loading for these particles. Drastic reduction of PT pressure by plastic straining, in addition to supporting DPBM and underlying theory, may transform the discovery of high-pressure phases of Si and other materials into economic technologies of their synthesis. Also, Si-II is retained at ambient pressure, and reverse Si-II→Si-I PT is obtained after plastic strain-induced direct transformation during unloading and holding at ambient pressure; these were never achieved before. For 100 nm Si, under torsion, an unknown sequence of PT Si-I → I + II → I + II + III is observed, and the coexistence of four phases, Si-I, II, III, and XI, is found. In addition, single-phase nano-Si-III and nanocomposite of two semiconducting phases Si-I + III were recovered after plastic deformation of 100 nm Si. All the above results demonstrate drastic differences between pressure-induced and strain-induced PTs and the possibility of manipulating transformation paths and developing advanced

https://doi.org/10.1038/s41467-024-51469-5

Table 1 | Summary of a sequence of PTs in Si with different particle sizes under hydrostatic and non-hydrostatic (plastic) compressions and torsion inside RDAC

Si PTM gasket	PT sequence, coexisting phases, and PT initiation pressures Hydrostatic compression *p* (GPa)						Phases at 10^{-4} GPa
Micron He S. S.	I + II + XI 13.5		I + XI 14.6	XI 15.3	-	V 16.5	XII + III
100 nm He S. S.	I + II + XI 16.2		II + XI 17.8	XI 18.1	-	V 19.3	XII + XII, I + III
30 nm He S. S.	-		I + XI 14.6	-	I + V 19.8	V 23.2	a
Si gasket anvil, run	**PT sequence, coexisting phases, and PT initiation pressures Non-hydrostatic compression *p* (GPa), *r* (μm)**						**Phases at 10^{-4} GPa**
Micron S. S. smooth, 1	I + II 2.6, 96	I + II + XI 10.4, 56	I + XI 14.5, 24	XI 15.2, 56	XI + V 15.7, 32	V 16.3, 16	XII + III
100 nm Cu smooth	I + II 0.6, 40	I + II + III 6.7, 40	I + II + XI 10.6, 0	II + XI 15.4, 20	-	V 17.5, 0	III
30 nm Cu smooth	I + II 4.9, 30	I + II + XI 10.4, 0	XI + V 13.2, 40	-	-	V 13.7, 0	I + II, II
Si gasket anvil, run	**PT sequence, coexisting phases, and PT initiation pressures Non-hydrostatic compression with shear *p* (GPa), *r* (μm), rotation angle (degrees)**						**Phases at 10^{-4} GPa**
100 Cu smooth, 1	I + II 0.3, 70 0°	I + II + III 0.6, 60 10°	I + II + III + XI 9.9, 0 0°	I + II + XI 12.2, 50 0°	XI + V 13.9, 20 0°	II + XI 12.6, 40 0°	XII + III
100 nm S. S. rough, 2	I + II 1.6, 30 0°	I + II + III 4.4, 40 24.6°	-	-	-	-	I + II, I + III, I + II + III + XII
100 nm S. S. rough, 3	I + II 3.5, 20 10.2°	-	-	-	-	-	I

PTM represents the pressure transmitting medium used for the hydrostatic XRD measurement; S.S. designates a stainless-steel gasket. The phase mixtures in the pressure released samples to 10^{-4} GPa are shown in the last column for each case. The Si particle size, PTM, gasket, anvil, and run number are provided in the first column for each case. All loading paths and names of experiments are shown in Supplementary Table 1.

scientific and applied fields of defect-induced material synthesis. Various other potential fundamental and technological applications are analyzed below.

Results

Prediction of the correlation between the particle size's direct and inverse Hall–Petch effects and initiation pressure for strain-induced phase transformation

It is corroborated in our analytical model[23], and phase-field simulations[33,34] that plastic strain-induced PT occurs by nucleation at the tip of a dislocation pileup as the strongest possible stress concentrator (DPBM). However, analytical theory[23] gives the wrong prediction on the grain size dependence on the PT pressure. According to the classical Eshelby model[29], all components of the stress tensor, $\boldsymbol{\sigma}$, at the tip of edge dislocation pileup, are $\boldsymbol{\sigma} \sim \tau l$, where τ is the applied shear stress limited by the yield strength in shear τ_y, l is the length of the dislocation pileup. Since l is traditionally limited by the fraction of the grain size d (e.g., $l = 0.5\,d$), the main conclusion in[23] was that the greater the grain size, the stronger the stress concentration and, consequently, the reduction in PT pressure. However, this is opposite to what we found in experiments, e.g., for α-ω PT in Zr[28]. To eliminate this contradiction, we will utilize the results of our phase-field[33,34], molecular dynamics[35], and concurrent atomistic-continuum simulations[36].

In contrast to the analytical solution utilized in[23], l is not related to the grain size since most dislocations are localized at the grain boundary, producing a step (superdislocation) (Supplementary Fig. 1), with effective length $l = Nb << d$, where b is the magnitude of the Burgers vector. Then we can use the stress field of a superdislocation, i.e., $\boldsymbol{\sigma} \sim \mu Nb/r$, where μ is the shear modulus, and r is the distance from the midpoint of a pileup. The number of dislocations equilibrated in a superdislocation in the first approximation, $N \sim \tau = \tau_y$ (see[36,37]), i.e., $\boldsymbol{\sigma} \sim \mu\tau_y b/r$. At the same time, τ_y increases with the decrease in d according to the Hall–Petch relationship[38], $\tau_y = \tau_0 + kd^{-0.5}$, where τ_0 and k are material parameters (Fig. 2a). Thus, $\boldsymbol{\sigma} \sim \mu(\tau_0 + kd^{-0.5})b/r$. That is why the stress concentration increases and p_ε^d decreases with decreasing grain size. This prediction is counterintuitive because, under hydrostatic conditions, the PT pressure increases with the grain size reduction[32,39], which we also confirm in Fig. 2a. However, for very small grain sizes, the above reasoning is not valid because the yield strength decreases with a further grain size reduction (the inverse Hall–Petch effect, Fig. 2a), and grain boundary sliding competes with the dislocation pileup formation. Then, based on the equation $\boldsymbol{\sigma} \sim \mu Nb/r$ and decreasing N with decreasing grain size, we conclude that the stress concentration decreases and p_ε^d increases with decreasing grain size in the range of validity of the inverse Hall–Petch effect. These qualitative predictions, including the crossover in PT pressure with decreasing grain

https://doi.org/10.1038/s41467-024-51469-5

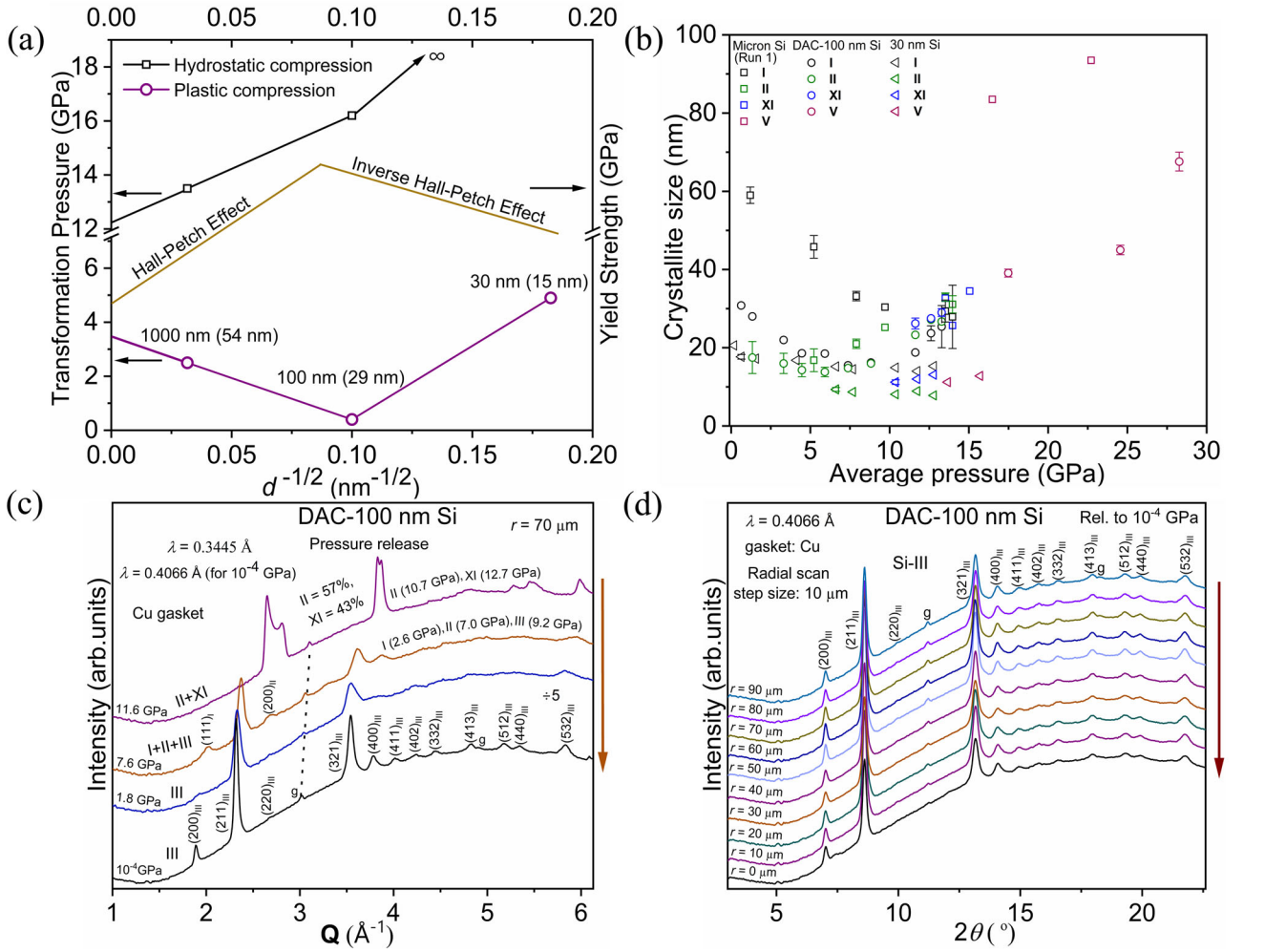

Fig. 2 | Particle-size dependence of phase transformation pressure, crystallite size effect *vs.* pressure, and synthesis of single-phase Si-III. a Experimental results on particle size dependence of the minimum Si-I→Si-II PT pressure under plastic straining and hydrostatic loading, and a schematic of particle size dependence of the yield strength according to the direct and inverse Hall–Petch effects. Numbers in parentheses are crystallite sizes at the initiation of the PT. The lines are drawn to guide the eye. The correlation between the particle size's direct and inverse Hall–Petch effects on the yield strength and the pressure for strain-induced PT is observed in accordance with the revisited DPBM. **b** The crystallite size *vs.* average pressure in I, II, XI, and V phases of Si for micron, 100 nm, and 30 nm particles are shown as square, circle, and triangle symbols, respectively. The error bar is excluded from all the figures if it overlaps with the symbols. **c** High-pressure synthesis of single-phase Si-III after compression in a DAC and released to the ambient from 11.6 GPa and $r = 70$ μm. Pure Si-III is observed at 1.8 GPa and is metastable at 10^{-4} GPa. The average pressure and pressure in each phase are shown on the leftmost and rightmost (in parentheses) sides of the figure, respectively; the phase fraction for each phase is shown in %; the same is done in all other figures, where relevant. A downward arrow on the right indicates pressure release. **d** The XRD patterns of nano Si-III along the sample radius with 10 μm step size at 10^{-4} GPa. Pure Si-III is observed in the entire region $r \leq 90$ μm.

size, will be confirmed experimentally (Fig. 2b), along with many other results (see below).

Experimental results

A summary of observed experimental results for hydrostatic loading, plastic compression in DAC, and torsion in RDAC for the three types of Si particles is presented in Table 1. Figure 2c, d show the high-pressure synthesis of single-phase nanograined Si-III. Figures 3a–d and 4a–d exhibit the high-pressure behavior of micron and 100 nm Si, initiation of PTs pressure, volume, and phase fraction distribution at 8.2 GPa and $r = 8$ μm for micron Si. The high-pressure behavior of 30 nm Si and the phase fractions of different types of Si under plastic compression are shown in Fig. 5a–d. High-pressure behavior of 100 nm Si, Si-I→Si-II PT initiation pressure for runs 1, 2, and 3 for 100 nm Si compressed and sheared inside the RDAC are provided in Fig. 6a–d. The initiation of Si-I→Si-III and Si-I→Si-II PTs for 100 nm and 30 nm Si under plastic compression and that of 100 nm Si with plastic compression and shear are shown in Fig. 7a–d. Numerous breakthrough results, which have never been reported in the literature, are listed in Table 1 and Figs. 2–9 and are discussed below.

For micron Si, the pressure reduction for Si-I→Si-II PT is from 13.5 to 2.6 GPa, by a factor of 5.2. The Si-II is observed at 3.3 GPa at $r = 0$ and 2.6 GPa close to the gasket (Fig. 4a, b). For 100 nm Si, plastic straining reduces Si-I→Si-II PT pressure from $p_h^d = 16.2$ GPa to $p_\varepsilon^d = 0.3$ GPa, i.e., by 54 times (Table 1, Figs. 2a, 6b, 7d). This is also 35 times below the phase equilibrium pressure $p_e = 10.5$ GPa. A slightly larger PT initiation pressure (0.6 GPa) for Si-I→Si-II PT in 100 nm Si under plastic compression compared with RDAC-Run1 (0.3 GPa) suggests that the sample was not packed well during sample loading (Table 1). For 30 nm particles, the PT pressure reduces from ∞ (since Si-II does not appear) to 4.9 GPa (Table 1, Figs. 2a, 7b). The Si-II is initiated at 6.6 GPa at $r = 0$ μm and 4.9 GPa at $r = 30$ μm (Figs. 5a, b, c, 7b).

Under shear, the Si-I→III PT initiates at 0.6 GPa for 100 nm Si (Fig. 7c), and PT Si-I→Si-II starts at 4.9 GPa for 30 nm Si (Fig. 7b), but both do not occur under hydrostatic loading for these particles. For 30 nm Si, Si-I→Si-II PT initiates between 5 and 6.6 GPa at $r = 0$ μm. For

https://doi.org/10.1038/s41467-024-51469-5

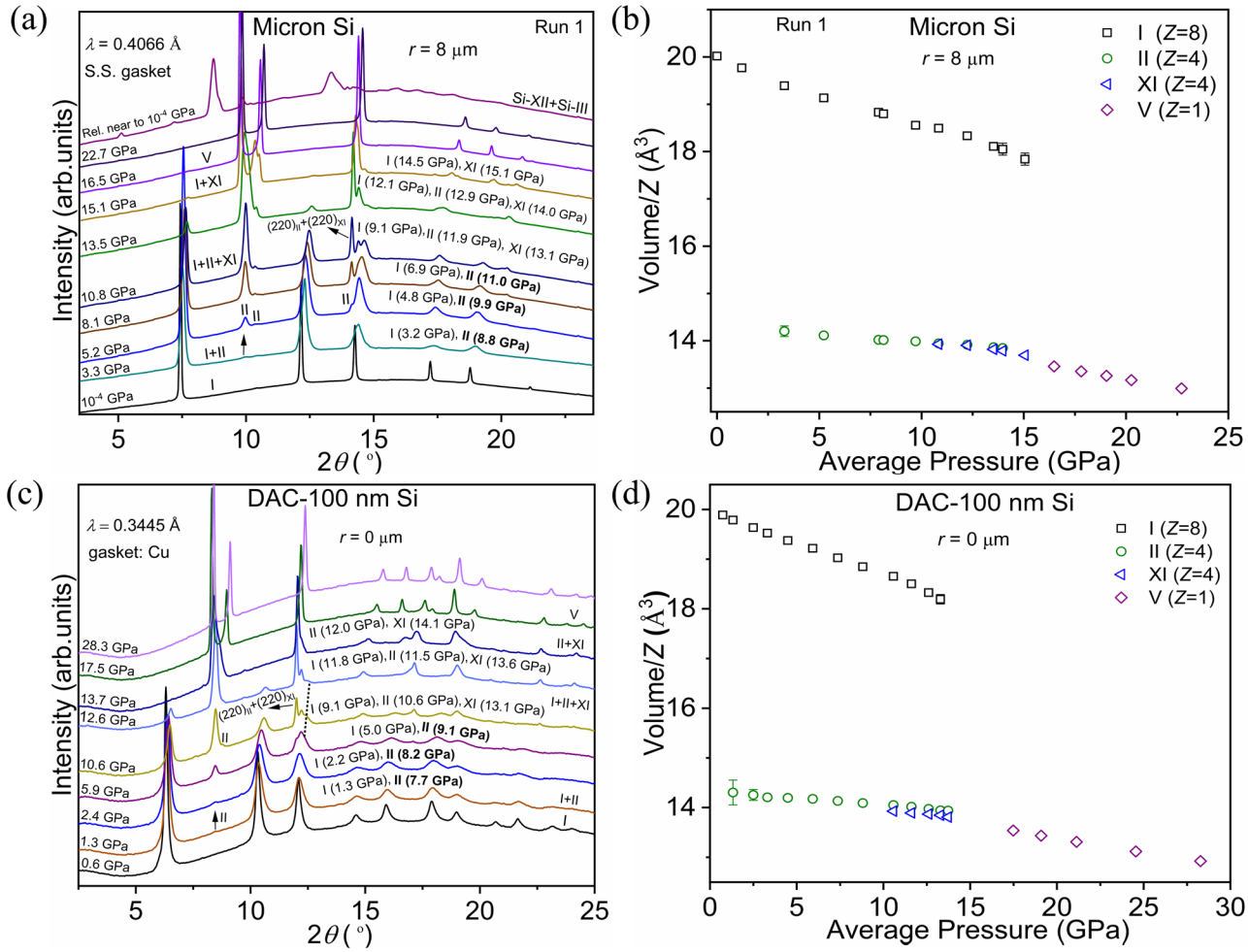

Fig. 3 | Plastic strain-induced PTs in micron and 100 nm Si under non-hydrostatic compression with smooth diamonds. a XRD of micron-size silicon at various pressures under non-hydrostatic compression at $r = 8$ μm from the sample center ($r = 0$). The arrow indicates the evolution of the (200) peak of the Si-II. The large pressure values of the Si-II compared to Si-I are shown in bold symbols here and in other figures. **b** Volume of the unit cell (V) over the number of atoms (Z) *vs.* average pressure for micron Si at $r = 8$ μm. **c** XRD patterns of 100 nm Si at various pressures at $r = 0$ μm. The arrow at 1.3 GPa represents the initiation of the Si-II phase. The indexing of Si-I, Si-II, Si-XI, and Si-V phases of micron and 100 nm Si are provided in Supplementary Figs. 5 and 6. **d** Volume/*Z* *vs.* average pressure for 100 nm Si.

100 nm Si, without shear, the Si-I→Si-III PT initiation pressure elevates to 6.7 GPa under plastic compression in DAC (Fig. 7a). The maximum phase fraction of Si-III for 100 nm Si is just 1% in DAC, whereas it is 6% in RDAC (Fig. 7a, Supplementary Table 2). Shear strains drastically reduce the initiation of Si-I→Si-III PT pressure and promote the evolution of the Si-III phase. Figure 2c, d show a completely different and much more economic PT pathway than in[9,10] to single-phase Si-III by unloading from 11.6 GPa within minutes at $r = 70$ μm and in the entire region $r \le 90$ μm, namely, Si-II + XI→Si-I + II + III→III, instead of the traditional Si-III synthetic path, Si-II→XII→III PT. We also noticed a traditional synthetic path along the sample diameter in some regions. For 100 nm Si, under torsion, PT occurs in the sequence Si-I→I + II→I + II + III (Table 1, Fig. 6a–c and Supplementary Tables 2–7), in contrast to different PT sequences suggested in[24,30,31] but not supported by the in situ XRD study. Nanocomposite of two semiconducting phases Si-I+Si-III in 100 nm Si, which may have valuable material properties, is retained after unloading from 4.7 GPa and rotation by 101.3° (see below). The coexistence of four Si phases, Si-I, II, III, and XI, is found (see below).

The effect of plastic strain is much weaker for the appearance of Si-XI. While for micron and 100 nm particles, Si-XI appears simultaneously with Si-II under hydrostatic loading, p_ε^d for Si-XI is by 7.8 and 9.6 GPa larger than Si-II with plastic straining (Table 1, Figs. 3, 6, and Supplementary Table 2). Thus, plastic straining can be used to separate phases. For 30 nm Si, PT pressure for the appearance of Si-XI reduces from 14.6 to 10.4 GPa (Table 1, Fig. 5a–c). The effect of plastic strain on the appearance of Si-V is weaker than for Si-II and Si-XI (Table 1 and Figs. 2b, 3, 5 and 6).

Our theoretical predictions on grain size dependence of p_ε^d are confirmed for the appearance of Si-II, i.e., there is a decrease in p_ε^d from micron to 100 nm particles and then an increase for 30 nm particles (Table 1, Figs. 2a, 3–6, Supplementary Tables 2–7). Compressed particles produce high-angle grain boundaries, representing the strongest obstacle for the dislocation pileup. Each particle possesses an internal grain/crystallite structure; the evolution of the crystallite size in different phases and particle sizes is presented in Fig. 2b. Since larger particle size corresponds to larger crystallite size at the initiation of PT, correlation in Fig. 2a can be presented in terms of the crystallite size as well. This is the only known and nontrivial correlation between strain-induced PTs and plasticity, which also supports the DPBM. Many more experiments are required to separate the effect of the particle and crystallite sizes. For the next PTs, to Si-XI and V, such correlation is not expected because PT occurs in a mixture of phases instead of a single phase, and phase interfaces may serve as additional obstacles for dislocation pileups; for 100 and 30 nm Si, the crystallite sizes are getting close or smaller than 20 nm and may determine material response. With increasing pressure, plastic strain and the crystallites'

https://doi.org/10.1038/s41467-024-51469-5

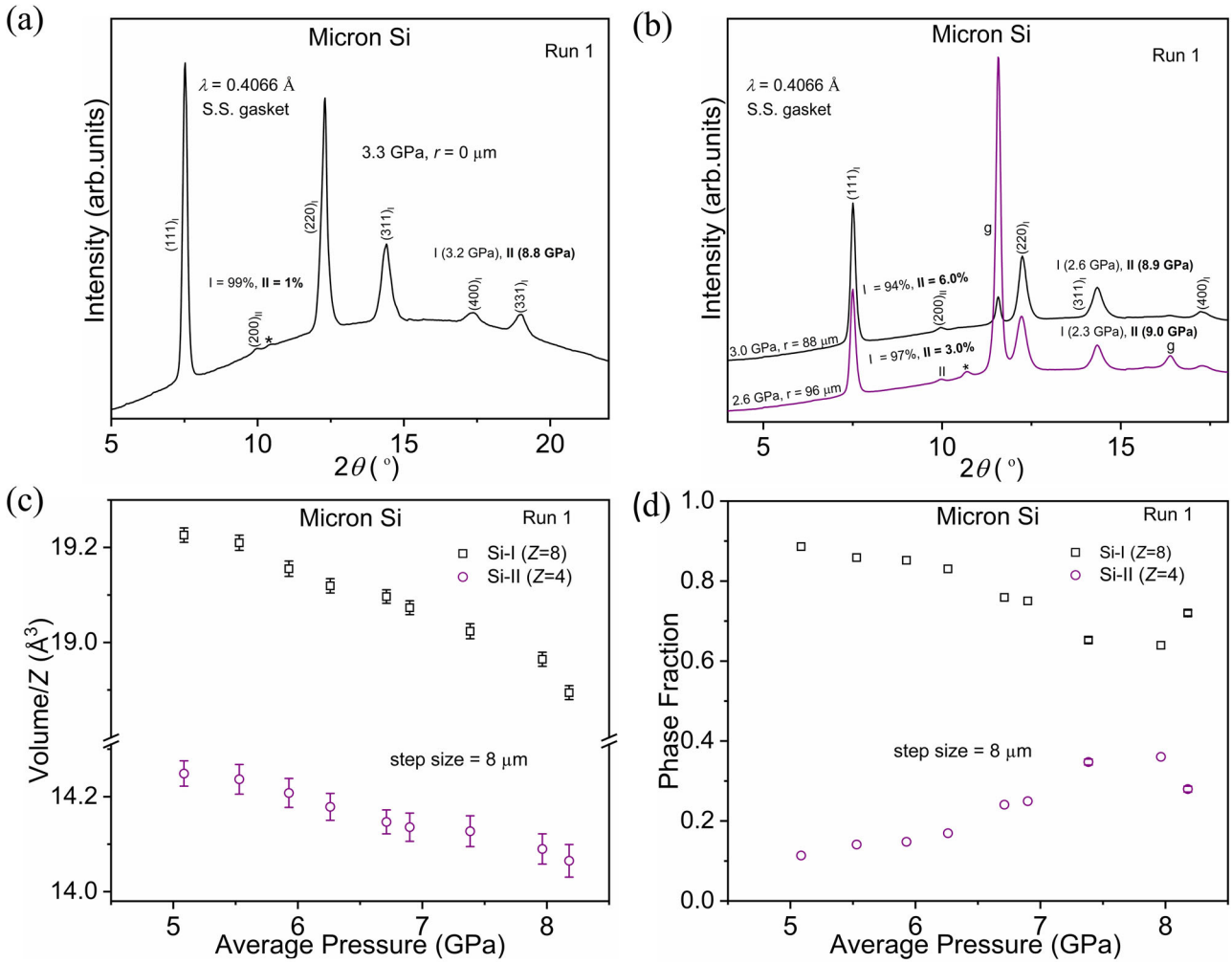

Fig. 4 | The XRD patterns, volume/Z, and phase fractions for strain-induced Si-I→II PT in micron particles for the sample plastically compressed inside a DAC using a stainless-steel gasket. (**a**) The initiation of strain-induced Si-I→II PT at (**a**) $r = 0$ μm and (**b**) away from the sample center. Symbol * represents an artifact (its origin is unknown). The volume/Z (**c**) and phase fraction (**d**) of Si-I and Si-II phases *vs.* pressure. XRD data is collected along the sample diameter with an 8 μm step size for 8.2 GPa at $r = 8$ μm. The volume of Si-I and Si-II phases monotonously increases from the sample center. The phase fraction of the Si-II phase is maximum near the sample center.

misorientation increase, making them a stronger obstacle for dislocation pileups and increasing their contribution to the size effect for PTs.

For PT I→II, $p_\varepsilon^d = 0.3$ GPa in 100 nm Si is the same for compression before torsion (Table 1 and Fig. 7d) and with torsion (Fig. 6b) in RDAC. Since the plastic strain tensor and its path are quite different for compression and torsion, this means that p_ε^d is independent of the plastic strain tensor and its path. Generally, rules of plastic flow and any related phenomena (PTs, defect generation, and grain size evolution) depend on the plastic strain tensor and its entire path, making numerous combinations of governing parameters. We obtained similar independence previously for α-ω PT in Zr[28,33], i.e., this may be a general rule for different classes of materials. This rule reveals that the physics of strain-induced PTs under compression in DAC and torsion in RDAC do not differ fundamentally, and strain-induced PTs can also be studied in DAC. Of course, RDAC has a strong advantage in allowing various controllable pressure-shear loading programs, particularly at constant pressure, close to p_ε^d, whereas in DAC, pressure significantly grows during compression. This is crucial for initiating and completing the desired PTs at low pressure.

Under the plastic shear of 100 nm Si in RDAC, Si-III initiates at 0.6 GPa, while it does not appear under hydrostatic compression (Table 1 and Fig. 7c)[39]. Similarly, for 30 nm Si, PT Si-I→Si-II starts at 4.9 GPa but does not occur under hydrostatic loading (Table 1 and Fig. 7b). These are two more examples of a drastic reduction in PT pressure for Si, which supports DPBM.

However, the most important result to support DPBM is that under plastic straining of 100 nm Si, pressure in small Si-II regions is ~5–7 GPa higher than in Si-I (Figs. 3c, 6a, b, c, 7c, d, and Supplementary Tables 5 and 6), while for pressure-induced PT, it is by 2.7 GPa lower due to 22% volume reduction[14,39] (Supplementary Table 12). Such high pressures in Si-II can be caused by strong stress concentrators due to dislocation pileup, in agreement with our phase-field simulations[33,34]. Indeed, for 30 nm Si, the difference is 1.4 GPa only (Fig. 5a), consistent with reduced dislocation activity in the region of the inverse Hall–Petch effect and increased PT pressure. With increasing pressure and the phase fraction c of Si-II for 100 nm Si, the difference in pressure between Si-I and Si-II reduces because the pressure in Si-II remains at 8–9 GPa for 100 nm Si. This is still much lower than $p_h^d = 16.2$ GPa; the remaining part of the local thermodynamic driving force comes from the work of non-hydrostatic stresses on deviatoric transformation strains (see[33,34] and Supplementary Discussion 3, 4). A similar difference in pressure in Si-I and Si-II is observed in micron Si (Figs. 3a, 4a, b) and Si-I and Si-III in 100 nm Si (Fig. 7c, Supplementary Fig. 7, and Supplementary Tables 5, 6).

https://doi.org/10.1038/s41467-024-51469-5

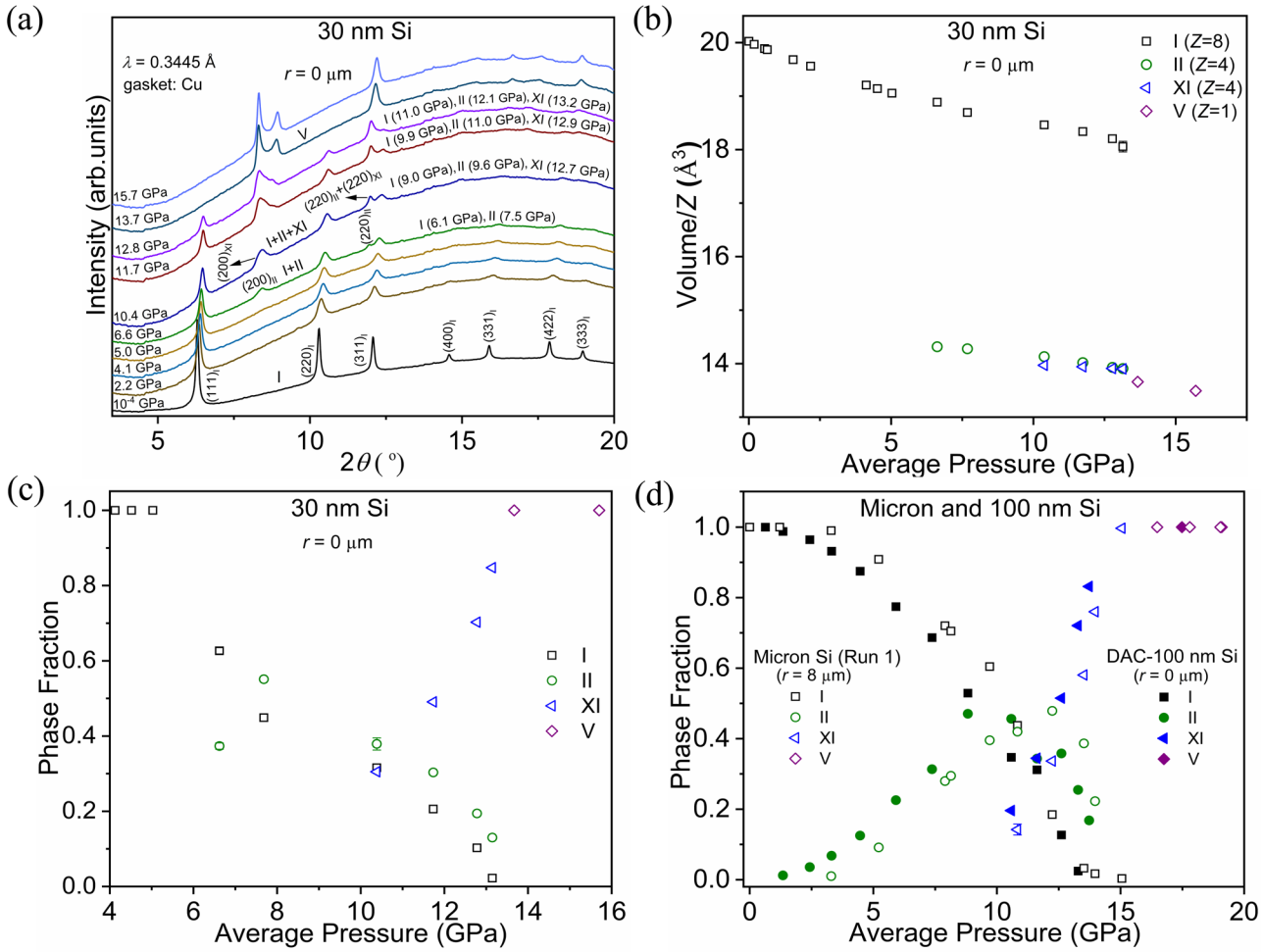

Fig. 5 | Plastic strain-induced PTs under non-hydrostatic compression in 30 nm Si at the sample center and phase fraction *vs.* pressure in micron, 100 nm, and 30 nm Si. a High-pressure XRD patterns of 30 nm Si at various pressures with smooth diamonds and Cu gasket. **b** Volume/*Z vs.* average pressure for 30 nm Si. **c** Phase fraction *vs.* average pressure for the 30 nm Si. **d** Phase fraction *vs.* average pressure for the micron Si and 100 nm Si.

One of the longstanding puzzles in Si is stabilizing the high-pressure Si-II phase at ambient conditions. In DAC experiments, Si-II was not retained at ambient conditions, even though the first-principle simulations[40,41] show the metastability of Si-II. Figure 8a–d show the retaining of micron, 30 nm, and 100 nm Si during and after the pressure release. Based on obtained experimental results and multiscale simulations[27], we were able to design a low-pressure compression-torsion loading path for 100 nm Si utilizing stainless steel and Cu gaskets and rough diamonds; we could retain a small amount of Si-II at normal pressure in several regions (Figs. 6d and 8d). During pressure reduction after a plastic compression experiment on 30 nm Si, we obtained Si-V→Si-II PT near ambient, and the pure Si-II phase was observed after the complete pressure release. A significant amount of Si-II was retained during Si-V→Si-II unloading of micron Si after plastic compression to 22.7 GPa (Fig. 8a). Retaining a large amount of Si-II will allow one to determine its properties under pressure, study it with traditional ex situ methods (SEM, TEM, mechanical properties, etc.), and eventually discover its potential applications, as happened with Si-III[10]. We have also observed reverse Si-II→Si-I PT both during unloading (Fig. 6d) and holding at ambient pressure for one week (Fig. 6d), which was never seen before since Si-II transforms to Si-III and XII during unloading. The Si-I + III and Si-I + II + III + XII phase coexistences in several regions under compression and shear in RDAC were also observed (Fig. 8d).

The evolution of the volume fraction of different phases (Figs. 4d, 5c, d and Supplementary Tables 2–4) is presented in terms of pressure. It also depends on the plastic strain, but they grow simultaneously during compression in DAC. These results do not show the minimum pressure to reach the given volume fraction because under torsion in RDAC away from the center, plastic strain and volume fraction could be increased at a fixed pressure, but this requires a special design of experiments[42–44], which is not a goal here. Indeed, for $\alpha \rightarrow \omega$ PT in Zr[28], for which, $p_\varepsilon^d = 1.2$ GPa, $p_h^d = 5.4$, GPa, $p_e = 3.4$ GPa, and the reverse PT is absent, the phase fraction $c = 0.91$ at the center under torsion by 30° at 2.4 GPa, the same as under compression to ~3.8 or 5.3 GPa for different pressure-plastic strain loadings. Under 40° and $r = 175$ μm, $c = 1$ at 2 GPa. Still, for 100 nm Si, for Si-II $c = 0.377$ at 9.0 GPa and 15° and $c = 0.54$ at 9.9 GPa and 82° at the sample center (Supplementary Table 2), while under hydrostatic conditions $c = 0.36$ is achieved at 16.2 GPa[39]. For 30 nm Si, $c = 0.55$ at 7.7 GPa for plastic compression (Fig. 5c), but $c = 0$ under any pressure during hydrostatic loading.

Discussion

Currently, no experimental technique is available to study DPBM for in situ strain-induced PTs under high pressure in DAC/RDAC because of insufficient spatial resolution, and averaging x-ray patterns over a sample thickness. Since they are strongly concentrated at the grain boundaries and are highly energetic, dislocation pileups (super-dislocations) become equilibrated by high external shear stresses. These dislocation pileups partially or completely disappear after releasing shear stresses and pressure and are undetectable in

https://doi.org/10.1038/s41467-024-51469-5

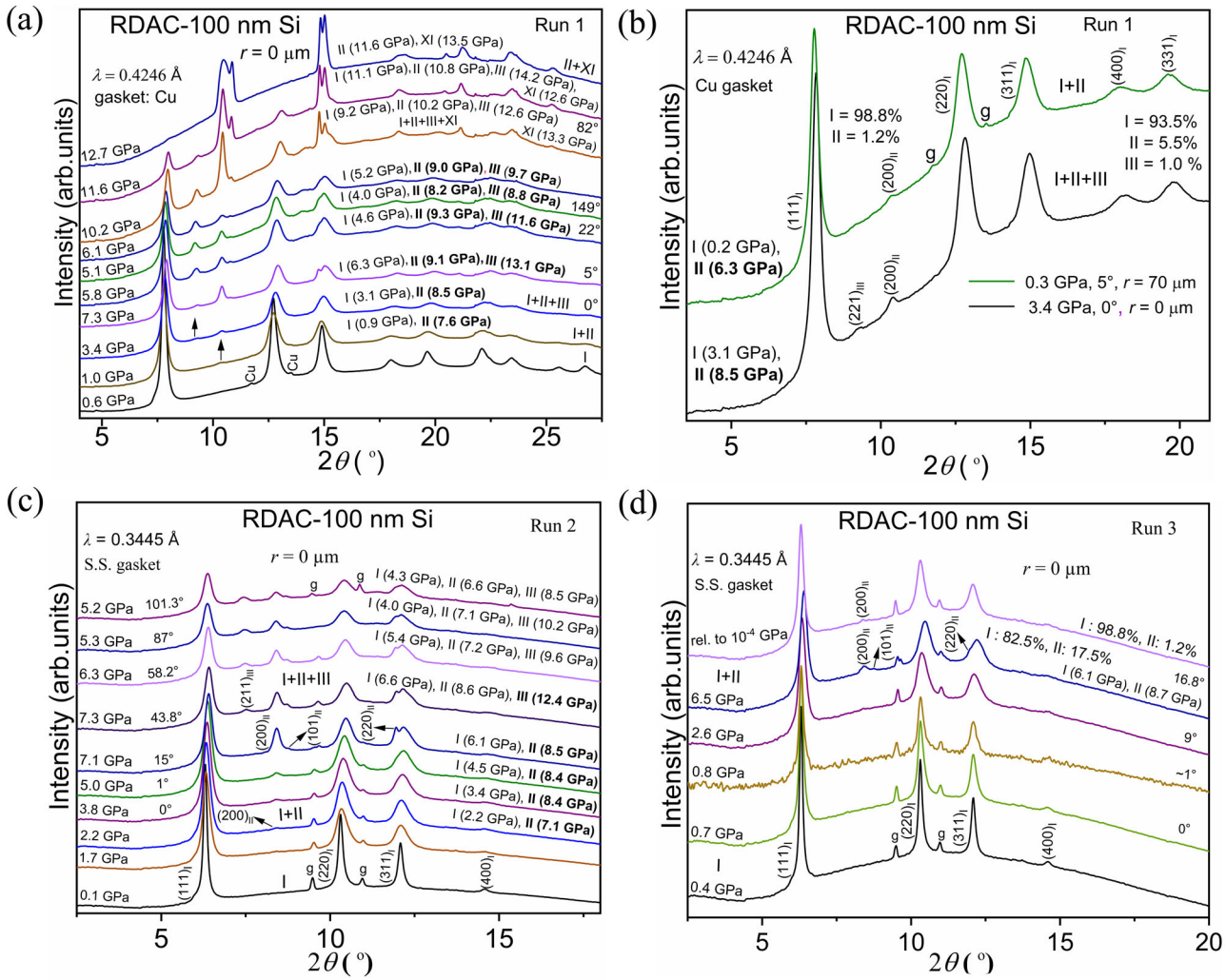

Fig. 6 | Plastic strain-induced PTs in 100 nm Si with torsion inside the RDAC. **a** XRD patterns for 100 nm Si within Cu gasket at various pressures and anvil rotations with smooth diamonds at $r = 0$ μm. The torsion is applied at 3.4 GPa and 6.1 GPa at $r = 0$ μm. The arrows represent the evolution of (200) and (211) peaks of the Si-II and Si-III phases, respectively. The indexing of Si-I, Si-II, Si-III, and Si-XI phases are provided in the Supplementary Figs. 7 and 9. **b** Initiation of Si-I→Si-II PT at 0.3 GPa, $r = 70$ μm and shear, 5°. The Si-I, Si-II, and Si-III phases coexist at 3.4 GPa, $r = 0$ μm, and shear, 0°. The same PT initiation pressure is obtained at $r = 60$ μm (for 1.1 GPa at $r = 0$); see Fig. 7d. **c** XRD patterns of 100 nm Si at various pressures and torsions with rough diamonds and S. S. gasket. The Si-II is initiated at 2.2 GPa at $r = 0$ and 1.6 GPa at $r = 30$ μm (Table 1). The piston side diamond anvil was continuously rotated up to 101.3° at 1 rotation per hour. **d** XRD patterns of 100 nm Si for selected pressures and torsions with rough diamonds at $r = 0$ with S. S. gasket. The sample was pressurized up to 0.7 GPa, and the shear was applied by continuously rotating one of the anvils up to 16.8° at 1 rotation per hour. The Si-II was initiated at 6.5 GPa at $r = 0$ and 3.5 GPa at $r = 50$ μm. The pressure was released to ambient from 6.5 GPa. A small amount (1.2%) of Si-II was retained under ambient conditions. Since the phase fraction of Si-II significantly reduces during pressure release, the reverse Si-II→Si-I PT was also observed.

numerous transmission electron microscopy studies of nanograined materials[11,12,45]. That is why the only way to confirm DPBM is to find strong indirect experimental corroborations. We advanced the DPBM model to eliminate the wrong grain size dependence of the PT pressure and predicted a correlation between the particle/crystallite size dependence of the PT pressure for strain-induced PT and direct and inverse Hall–Petch relationships for yield strength. Since we confirmed this correlation experimentally and the particle size dependence of the PT pressure for strain-induced PT and pressure-induced PT is very different, our results strongly support DPBM. We observed a strong reduction in PT pressures for the appearance of Si-II and III due to plastic deformation, which the dislocation pileup mechanism can plausibly explain.

Most importantly, under plastic straining, pressure in small Si-II regions is ~5–7 GPa higher than in Si-I for micron and 100 nm Si, clearly showing strong stress concentration, while for pressure-induced PT, it is by 2.7 GPa lower due to 22% volume reduction. For 30 nm Si, the increase for strain-induced PT is 1.4 GPa only, consistent with the reduced dislocation activity in the region of the inverse Hall–Petch effect and the increased PT pressure. A similar difference in pressure in Si-I and Si-III is observed in 100 nm Si.

Theoretical pressure for barrierless nucleation strongly depends on the magnitude and mode of the deviatoric (non-hydrostatic) stresses[41]. Strong heterogeneity of the stresses around the tip of the dislocation pileup[23,29] explains the appearance of multiple phases in different regions and the sequence of PTs, which differs from that under hydrostatic conditions. The weak effect of plastic straining on some PTs does not contradict DPBM because, for some phases, grain boundaries may be transparent to the dislocations responsible for plasticity; dislocations cannot pileup and promote PTs. This is, e.g., the case for screw dislocations in Si-I[46]. Also, the crystallite size of Si-I and II in strain-induced PT to Si-V and Si-XI is getting so small that it belongs to the region of the inverse Hall–Petch effect and increases the PT pressure.

https://doi.org/10.1038/s41467-024-51469-5

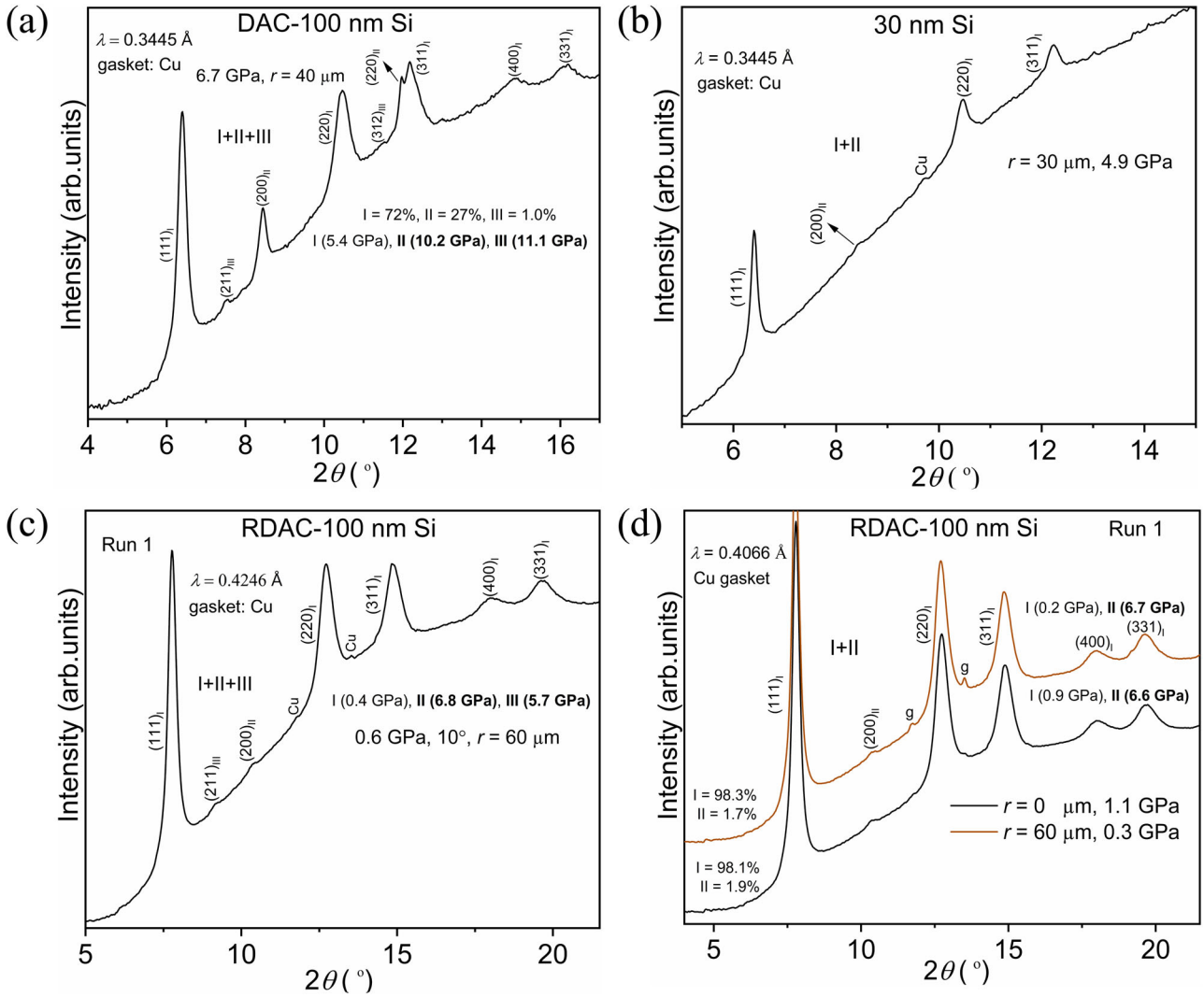

Fig. 7 | Initiation of Si-I→Si-III and Si-I → Si-II PTs in 100 nm Si and 30 nm Si under non-hydrostatic compression and shear. a Initiation of Si-I→Si-III PT in 100 nm Si under non-hydrostatic compression inside a DAC. The average pressure of the sample at $r = 40$ μm is 6.7 GPa. **b** Initiation of Si-I→II PT for 30 nm particles at 4.9 GPa and $r = 30$ μm. The sample was compressed under non-hydrostatic conditions inside a DAC using a Cu gasket. "Cu" represents the gasket peak. **c** Initiation of Si-I→Si-III PT pressure in Si-III phase of 100 nm Si with non-hydrostatic compression and shear inside RDAC. **d** The XRD pattern of 100 nm Si compressed and sheared inside an RDAC at 60 μm from the sample center with a shear of 10°. The initiation of Si-I→Si-II PT at 0.3 GPa in RDAC but before torsion; g is the gasket peak.

Drastic reduction in PT pressures due to plastic deformation and its nontrivial dependence on the particle size, as well as change in transformation paths and ability to manipulate them open (i) basic direction in the multiscale theoretical description of these phenomena, e.g., by further developing approaches reviewed in[27], and (ii) applied direction in developing the scientific foundation for plastic strain- and defect-induced synthesis and retrieving the desired nanostructured pure phases or mixture of phases (nanocomposites) with optimal electronic, optical, and mechanical properties. This can be done at low pressure, room temperature, in a short time, and without a catalyst. Due to multiple PTs, Si represents an ideal model material for developing similar approaches for other strong and brittle semiconductors (Ge, Si_xGe_{1-x}, GaAs, InSb, GaSb, etc.), graphite-diamonds (cubic, hexagonal, orthorhombic, etc.) and similar BN systems. Nanocomposites may vary with increasing pressure from the high-pressure phase near the tip of the dislocation pileup or grain boundary and other 2D obstacles (1D and 2D complexions[47–49]), or 3D inclusions or multiconnected matrix type composites, and being two-phase or multiphase. Some phases may survive at low pressure by encapsulation (pre-straining) by the low-pressure phase. Desired single phases may be extracted from a composite using special technology, e.g., for extracting diamonds from the mixture with a metal catalyst and residual graphite during industrial diamond synthesis[50].

In particular, while obtaining pure Si-III after quenching from 14 GPa and 900 K over three days or in Na-Si system at 9.5 GPa and 1000 K[9] or by two compression/slow (within 4 hours) decompression cycles to 13 GPa and room temperature[51], it was mentioned in[9] as a promising result that Si-III appeared at 7 GPa and 1000 K. We obtained Si-III within a few minutes at 0.6 GPa at room temperature with an anvil rotation of 5°. Various synthetic compression-torsion-unloading paths can be developed to obtain pure Si-III at ambient pressure. Since the transformation rate is proportional to the strain rate[23,27], it can be increased by increasing the rotation rate. Then, single-phase Si-IV can be obtained from Si-III by annealing. Another result is obtaining pure Si-III in the entire region $r \le 90$ μm after compression of 100 nm Si to 11.6 GPa (at $r = 70$ μm) and unloading within several minutes (Fig. 2b, c); it is already more economical than the above methods[9,51]. Nanocomposite of two semiconducting phases Si-I+Si-III in 100 nm Si retained after unloading from 5.2 GPa and rotation by 101.3° may have useful material properties. We obtained Si-I + II + III + XI phase

https://doi.org/10.1038/s41467-024-51469-5

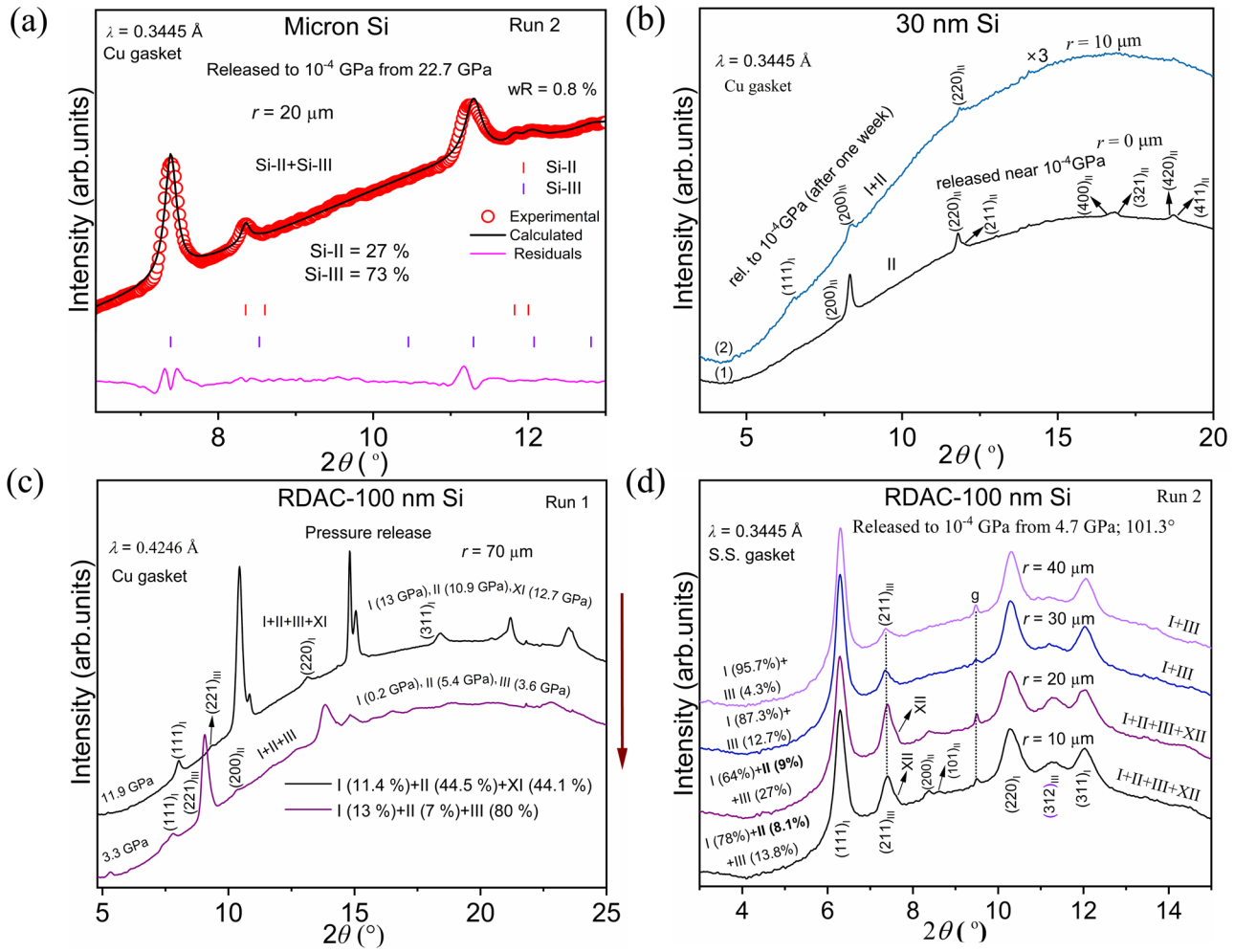

Fig. 8 | Recovering Si-II, Si-III, and Si-XII phases after non-hydrostatic compression of micron-size and 30 nm Si inside a DAC and compression and shear of 100 nm Si inside RDAC. a Recovering Si-II after non-hydrostatic compression of micron-size Si within Cu gasket inside a DAC. Rietveld refinement of micron-size silicon at $r = 20$ μm after non-hydrostatic compression up to 22.7 GPa followed by pressure release to the ambient. Recovery of the Si-II phase was not reported previously in static high-pressure experiments. wR is the weighted profile *R*-factor **b** The retaining of Si-II at ambient pressure and reverse Si-II→Si-I in 30 nm Si after holding the sample at ambient conditions. XRD patterns of 30 nm Si sample after non-hydrostatic compression up to 15.7 GPa and complete pressure release are presented, (1) immediately after pressure release to 10^{-4} GPa (ambient) and (2) after one week. The ×3 indicates that the intensity of XRD pattern (2) is magnified thrice. **c** XRD patterns of pressure released sample after compression and shear inside RDAC (run 1) at $r = 70$ μm and 11.9 GPa and released to 3.3 GPa. The pressure at the sample center before release is 12.7 GPa (Fig. 6a). A small fraction of Si-III is seen at 11.9 GPa, which is excluded during refinement. The vertical arrow represents the pressure release at $r = 70$ μm and 11.6 GPa. **d** XRD patterns of pressure released sample compressed and sheared at 5.2 GPa and 101.3° inside RDAC (run 2). Nanocomposite of two semiconducting phases Si-I+Si-III at $r = 30$, 40 μm and Si-I+Si-II+Si-III+Si-XII phase coexistence at $r = 10$ and 20 μm are observed. Four-phase fitting did not provide a reliable phase fraction of Si-XII; therefore, it is not presented. The dotted lines denote $(211)_{III}$ and gasket (g) peaks at different sample positions. A shoulder peak right to the $(211)_{III}$ is from the Si-XII phase.

coexistence and a significant amount of Si-II (38.8%) at 7.4 GPa and a small shear of 5° (Fig. 9a, b).

The obtained results can also be used for quantitative modeling and optimization of the surface processing (polishing, turning, scratching, etc.) of strong brittle semiconductors and developing regimes of ductile machining by utilizing PT to ductile (Si-II and a-Si) phases[52,53]. The current molecular dynamics modeling on cutting polycrystalline Si-I shows the formation of Si-II and a-Si at ~10 GPa under shear, i.e., close to the values for a single crystal under hydrostatic conditions[53]. The main reason is that atomistic simulations are limited to very small grain sizes, which are in the range of the validity of the inverse Hall–Petch effect, like for 30 nm Si in Fig. 2b. For 100 nm particles, this pressure can be drastically reduced to sub-GPa (Fig. 2a and Table 1).

Since the PTs in Si were typically obtained at pressures greater than 10 GPa, they were neglected in typical normal and relatively low-pressure applications. The observed very low PT pressures warn that some PTs may occur, e.g., in NEMS/MEMS, during contact interactions and friction, and should be taken into account or/and avoided.

Our results, especially with rough diamonds, can be scaled up to a larger volume using high-pressure torsion with rotating metallic/ceramic anvils[11,12,25]. RDAC experiments can also be used for in situ studying processes occurring during high-pressure torsion. Traditional high-pressure torsion cannot be monitored in situ; it is studied ex situ after completing the entire or part of the process and unloading. Since Si phases after unloading differ from those during loading (Table 1), the final product does not characterize any PT during the loading. Even for other material systems without PTs during pressure release, the in situ study is much more representative, better characterized, and precise because it allows getting many more experimental points at different loadings, characterizing parameters (e.g., pressure) in each point (instead of force divided by

https://doi.org/10.1038/s41467-024-51469-5

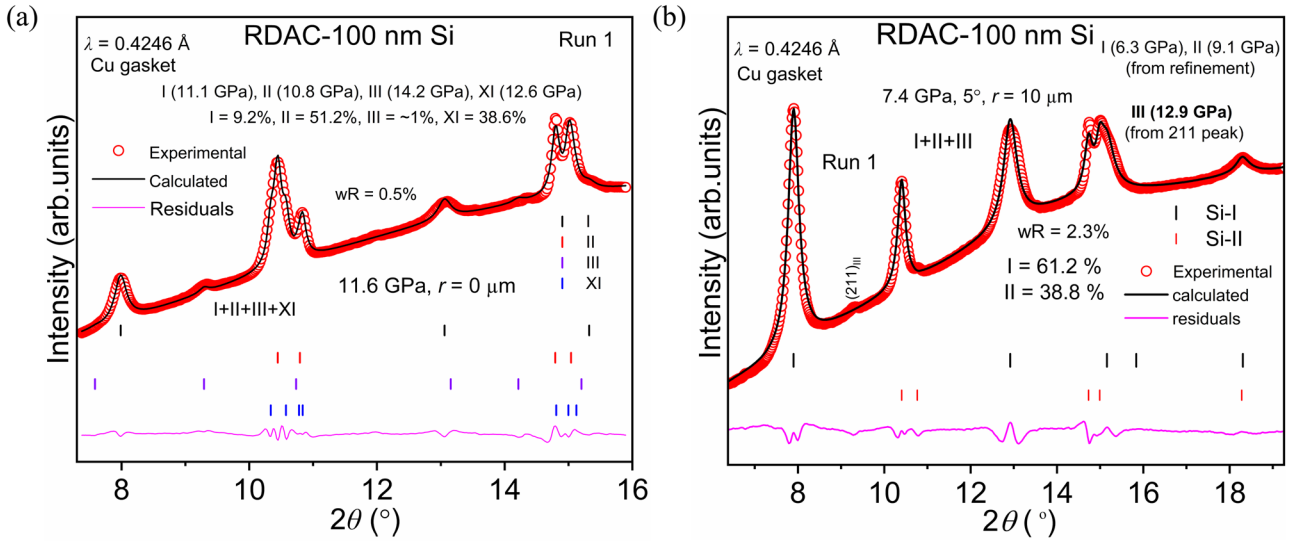

Fig. 9 | Observation of the coexistence of Si-I, Si-II, Si-III, and Si-XI phases and producing a significant amount of Si-II of 100 nm Si within Cu gasket at low pressure. a Rietveld refinement of XRD data at $r = 0$ μm after compression and shear inside an RDAC. The average pressure in the sample is 11.6 GPa. The pressure and phase fractions of all the phases are shown. **b** Rietveld refinement of 100 nm Si after compression at 7.4 GPa and a small shear of 5° inside an RDAC. A significant amount of Si-II is observed at $r = 10$ μm. Since the Si-III peaks are very weak, the Si-III phase is excluded during the refinement.

total area), and avoids damage of the brittle materials at normal conditions.

Methods

Materials

Hydrostatic experiments with He pressure transmitting medium (PTM) and plastic compressions (without PMT) in DAC and torsion in the RDAC were conducted on Si with particle sizes of $d = 1$ μm, 100 nm, and 30 nm. Single crystal silicon purchased from Sigma-Aldrich was powdered to 1 μm size fine powders by grounding with a pestle and mortar. The Si powder with <100 nm particle size (TEM) and ≥98% pure sample was purchased from Sigma-Aldrich (CAS No.: 7440-21-3). Also, Si powder with 30 nm particle size was purchased from Meliorum Technologies, Inc.

Synchrotron X-ray diffraction

The high-pressure experiments were carried out using symmetric-type DAC and RDAC with 230, 300, and 400 μm culet diameters. We have used both polished and rough diamonds[54] for this study, and the description of the RDAC used for run 1 can be found in[55]. The RDAC run 2 and 3 experiments for the 100 nm Si were conducted using RDAC from DAC Tools, LLC, IL. Both stainless steel (S. S.) and Cu gaskets with an initial thickness of 70–153 μm were utilized with hole (sample) diameters of 120–220 μm. The non-hydrostatic sample loading was carried out with Cu and S. S. gaskets; no PTM was used. While a stronger S. S. gasket and smaller initial sample thickness allow higher pressure - smaller plastic strain loading trajectory, a weaker Cu gasket, and larger initial sample thickness ensures larger plastic strain at relatively low pressure. A drastic reduction in PT initiation pressure was achieved using a Cu gasket with 150 μm thickness. All the high-pressure X-ray diffraction experiments were carried out at the 16-ID-B beam line, HPCAT, utilizing Advanced Photon Source with X-ray wavelengths 0.4066 Å, 0.4246 Å, and 0.3445 Å. The X-ray beam with spot size 5 μm × 4 μm was scanned along the sample diameter with step sizes 8 μm for micron Si and 10 μm for all other data at various pressures at the sample center. All data, including the pressure we present for any sample point, are obtained from the same point. The data from different sample points can be distinguished by the corresponding r values (radial distance from the sample center in μm). The XRD patterns were refined using GSAS-II software to extract the lattice parameters, crystallite size, and volume fractions of Si phases using the Rietveld refinement method[56]. The 2D XRD image was converted to a 1D pattern using dioptase software[57]. The spherical harmonics texture model was used to fit the high-pressure Si phases. The CIF files for plotting the Si-I and Si-V unit cells were taken from the ICSD database with codes (Si-I: 51688 and Si-V: 52456). The lattice parameters and Wyckoff positions of Si-II, Si-XI, Si-III, and Si-XII phases are taken from[13,58,59]. The best fit for Si-II is obtained with the Wyckoff position (4b): $x = 0$, $y = 0.25$ and $z = 3/8$. The crystal structures were plotted using VESTA. The source data for the XRD study is provided.

Pressure Determination

The supplementary Table 13 contains material parameters of the third-order Birch-Murnaghan EOS (BM3 EOS)[60] used to determine pressure in all phases and particles taken from[39]. They were obtained using He PTM[61] and a ruby pressure scale[62], and a simple iterative procedure was developed to extract the Si-II and Si-XI EOS from the P-V data containing a mixture of phases with different pressures in each phase. For Si-II, the first principles simulation results from[41] were utilized to extend EOS to zero pressure, as S-II does not exist under hydrostatic loading below 13.5 GPa. This is the best that can be currently done. While a possible error can change the pressure in Si-II on 100 nm Si by 1 GPa and the maximum/minimum error in the average pressure by 0.54/0.01 GPa, this will not change any conclusion because the pressure in Si-II is 5–7 GPa higher than in Si-I. The PT initiation pressures for various PT sequences are taken from different regions of the same sample (Table 3). The Si-I, Si-II, Si-III, Si-XI, and Si-V phases are designated as I, II, III, XI, and V, respectively. The subscripts I, II, XI, and V of the (hkl) Bragg planes represent the Bragg planes of the Si-I, Si-II, Si-XI, and Si-V phases, respectively. Pressure at each sample point in each phase was determined using the measured volume of Si phases and equations of state of Si phases. We report pressure in each phase and pressure averaged over all phases. The average (actual) pressure is the sum of the product of the phase fraction and the pressure in each phase. In Fig. 4c, d, the XRD data was collected along the culet diameter with an 8 μm step size. The volume and phase fractions of XRD data at each point equidistance from the sample center on either side are averaged to plot volume/Z and phase fraction versus pressure from $r = 0$ to 72 μm.

Data availability

Source data are provided with this paper.

References

1. Rödl, C. et al. Wurtzite silicon as a potential absorber in photovoltaics: tailoring the optical absorption by applying strain. *Phys. Rev. B* **92**, 045207 (2015).
2. Craighead, H. G. Nanoelectromechanical systems. *Science* **290**, 1532–1535 (2000).
3. Wippermann, S., He, Y., Vörös, M. & Galli, G. Novel silicon phases and nanostructures for solar energy conversion. *Appl. Phys. Rev.* **3**, 040807 (2016).
4. Cho, C.-H., Aspetti, C. O., Park, J. & Agarwal, R. Silicon coupled with plasmon nanocavities generates bright visible hot luminescence. *Nat. Photonics* **7**, 285–289 (2013).
5. Hwang, G. C. et al. Pressure-driven phase transitions and reduction of dimensionality in 2D silicon nanosheets. *Nat. Commun.* **9**, 5412 (2018).
6. Zeng, Z. Q. et al. Origin of plasticity in nanostructured silicon. *Phys. Rev. Lett.* **124**, 185701 (2020).
7. Chrobak, D. et al. Deconfinement leads to changes in the nanoscale plasticity of silicon. *Nat. Nanotechnol.* **6**, 480–484 (2011).
8. Rodgers, P. Silicon goes thermoelectric. *Nat. Nanotechnol.* **3**, 76–76 (2008).
9. Kurakevych, O. O. et al. Synthesis of bulk BC8 silicon allotrope by direct transformation and reduced-pressure chemical pathways. *Inorg. Chem.* **55**, 8943–8950 (2016).
10. Zhang, H. et al. BC8 silicon (Si-III) is a narrow-gap semiconductor. *Phys. Rev. Lett.* **118**, 146601 (2017).
11. Ikoma, Y. et al. Phase transformation and nanograin refinement of silicon by processing through high-pressure torsion. *Appl. Phys. Lett.* **101**, 121908 (2012).
12. Ikoma, Y. et al. Fabrication of nanograined silicon by high-pressure torsion. *J. Mater. Sci.* **49**, 6565–6569 (2014).
13. McMahon, M., Nelmes, R., Wright, N. & Allan, D. Pressure dependence of the Imma phase of silicon. *Phys. Rev. B* **50**, 739 (1994).
14. Anzellini, S. et al. Quasi-hydrostatic equation of state of silicon up to 1 megabar at ambient temperature. *Sci. Rep.* **9**, 15537 (2019).
15. Hu, J. Z., Merkle, L. D., Menoni, C. S. & Spain, I. L. Crystal data for high-pressure phases of silicon. *Phys. Rev. B* **34**, 4679 (1986).
16. Fan, L., Yang, D. & Li, D. A review on metastable silicon allotropes. *Materials* **14**, 3964 (2021).
17. Haberl, B., Strobel, T. A. & Bradby, J. E. Pathways to exotic metastable silicon allotropes. *Appl. Phys. Rev.* **3**, 040808 (2016).
18. Valentini, P., Gerberich, W. & Dumitrică, T. Phase-transition plasticity response in uniaxially compressed silicon nanospheres. *Phys. Rev. Lett.* **99**, 175701 (2007).
19. He, Y. et al. In situ observation of shear-driven amorphization in silicon crystals. *Nat. Nanotechnol.* **11**, 866–871 (2016).
20. Wang, Y.-C. et al. In situ TEM study of deformation-induced crystalline-to-amorphous transition in silicon. *NPG Asia Mater.* **8**, e291–e291 (2016).
21. Kiran, M. S., Haberl, B., Bradby, J. E. & Williams, J. S. *Nanoindentation of Silicon and Germanium*, in *Semiconductors and Semimetals* Vol. 91 165-203 (Elsevier, 2015).
22. Domnich, V., Ge, D. & Gogotsi, Y. *Indentation-induced phase transformations in semiconductors*, in *High-Pressure Surface Science and Engineering* 381-442 (CRC Press, 2019).
23. Levitas, V. I. High-pressure mechanochemistry: conceptual multiscale theory and interpretation of experiments. *Phys. Rev. B* **70**, 184118 (2004).
24. Blank, V. D. & Estrin, E. I. *Phase transitions in solids under high pressure*. (Crc Press, 2013).
25. Edalati, K. & Horita, Z. A review on high-pressure torsion (HPT) from 1935 to 1988. *Mater. Sci. Eng.: A* **652**, 325–352 (2016).
26. Gao, Y. et al. Shear driven formation of nano-diamonds at sub-gigapascals and 300 K. *Carbon* **146**, 364–368 (2019).
27. Levitas, V. I. High-pressure phase transformations under severe plastic deformation by torsion in rotational anvils. *Mater. Trans.* **60**, 1294–1301 (2019).
28. Pandey, K. K. & Levitas, V. I. In situ quantitative study of plastic strain-induced phase transformations under high pressure: Example for ultra-pure Zr. *Acta Materialia* **196**, 338–346 (2020). Supporting raw data.
29. Anderson, P. M., Hirth, J. P. & Lothe, J. *Theory of dislocations*. (Cambridge University Press, 2017).
30. Alexandrova, M. M., Blank, V. D. & Buga, S. G. Phase Transitions in Ge and Si under Shear Strain under Pressure up to 12 GPa and P-T-Diagrams of these Elements. *Solid State Phys.* **35**, 1308–1317 (1993).
31. Blank, V. & Kulnitskiy, B. Crystallogeometry of polymorphic transitions in silicon under pressure. *High. Press. Res.* **15**, 31–42 (1996).
32. Xuan, Y. et al. Pressure-induced phase transitions in nanostructured silicon. *J. Phys. Chem. C.* **124**, 27089–27096 (2020).
33. Levitas, V. I. & Javanbakht, M. Phase transformations in nanograin materials under high pressure and plastic shear: nanoscale mechanisms. *Nanoscale* **6**, 162–166 (2014).
34. Javanbakht, M. & Levitas, V. I. Phase field simulations of plastic strain-induced phase transformations under high pressure and large shear. *Phys. Rev. B* **94**, 214104 (2016).
35. Chen, H., Levitas, V. I. & Xiong, L. Amorphization induced by 60° shuffle dislocation pileup against different grain boundaries in silicon bicrystal under shear. *Acta Materialia* **179**, 287–295 (2019).
36. Peng, Y. et al. Effect of a micro-scale dislocation pileup on the atomic-scale multi-variant phase transformation and twinning. *Computational Mater. Sci.* **230**, 112508 (2023).
37. Peng, Y. et al. An Atomistic-to-Microscale Computational Analysis of the Dislocation Pileup-induced Local Stresses near an Interface in Plastically Deformed Two-phase Materials. *Acta Materialia* **226**, 117663 (2022).
38. Voyiadjis, G. Z. & Yaghoobi, M. *Size effects in plasticity: from macro to nano*. (Academic Press, 2019).
39. Yesudhas, S., Levitas, V.I., Lin, F., Pandey, K. K., & Somayazulu, M. Effect of particle size on the phase transformation behavior and equation of state of Si under hydrostatic loading. *arXiv:2402.15092*
40. Gaál-Nagy, K. & Strauch, D. Phonons in the β-tin, Imma, and sh phases of silicon from ab initio calculations. *Phys. Rev. B* **73**, 014117 (2006).
41. Zarkevich, N. A., Chen, H., Levitas, V. I. & Johnson, D. D. Lattice instability during solid-solid structural transformations under a general applied stress tensor: Example of Si I→ Si II with metallization. *Phys. Rev. Lett.* **121**, 165701 (2018).
42. Feng, B. & Levitas, V. I. Effects of the gasket on coupled plastic flow and strain-induced phase transformations under high pressure and large torsion in a rotational diamond anvil cell. *J. Appl. Phys.* **119**, 015902 (2016).
43. Feng, B., Levitas, V. I. & Li, W. FEM modeling of plastic flow and strain-induced phase transformation in BN under high pressure and large shear in a rotational diamond anvil cell. *Int. J. Plasticity* **113**, 236–254 (2019).
44. Levitas, V. I., Ma, Y., Hashemi, J., Holtz, M. & Guven, N. Strain-induced disorder, phase transformations and transformation induced plasticity in hexagonal boron nitride under compression and shear in a rotational diamond anvil cell: in-situ X-ray diffraction study and modeling. *J. Chem. Phys.* **125**, 044507 (2006).
45. Edalati, K. et al. Nanomaterials by severe plastic deformation: review of historical developments and recent advances. *Mater. Res. Lett.* **10**, 163–256 (2022).
46. Chen, H., Levitas, V. I. & Xiong, L. Slip of shuffle screw dislocations through tilt grain boundaries in silicon. *Comput. Mater. Sci.* **1**, 132–135 (2019).

47. Luo, J. Computing grain boundary "phase" diagrams. *Interdiscip. Mater.* **2**, 137–160 (2023).
48. Baram, M., Chatain, D. & Kaplan, W. D. Nanometer-thick equilibrium films: the interface between thermodynamics and atomistics. *Science* **332**, 206 (2011).
49. Kuzmina, M., Herbig, M., Ponge, D., Sandlöbes, S. & Raabe, D. Linear complexions: confined chemical and structural states at dislocations. *Science* **349**, 1080–1083 (2015).
50. Novikov, N. V., Fedoseev, D. V., Shul'zhenko, A. A. and Bogatyreva, G. P. Diamond synthesis, Naukova Dumka, Kiev, 1987.
51. Li, X., Li, Z., Yang, K. & He, D. Phase-pure bulk BC8 silicon prepared through secondary phase transition method under high pressure. *Mater. Lett.* **262**, 127195 (2020).
52. Patten, J. A., Cherukuri, H. & Yan, J. *Ductile-regime machining of semiconductors and ceramics*, in *High-Pressure Surface Science and Engineering* 543-632 (CRC Press, 2019).
53. Goel, S., Luo, X., Agrawal, A. & Reuben, R. L. Diamond machining of silicon: a review of advances in molecular dynamics simulation. *Int. J. Mach. Tools Manuf.* **88**, 131–164 (2015).
54. Lin, F., Levitas, V. I., Pandey, K. K., Yesudhas, S. & Park, C. In-situ study of rules of nanostructure evolution, severe plastic deformations, and friction under high pressure. *Mater. Res. Lett.* **11**, 757–763 (2023).
55. Novikov, N., Shvedov, L., Krivosheya, Y. N. & Levitas, V. New automated shear cell with diamond anvils for in situ studies of materials using X-ray diffraction. *J. Superhard Mater.* **37**, 1–7 (2015).
56. Toby, B. H. & Von Dreele, R. B. GSAS-II: the genesis of a modern open-source all purpose crystallography software package. *J. Appl. Crystallogr.* **46**, 544–549 (2013).
57. Prescher, C. & Prakapenka, V. B. DIOPTAS: a program for reduction of two-dimensional X-ray diffraction data and data exploration. *High. Press. Res.* **35**, 223–230 (2015).
58. Kasper, J. S. & Richards, S. M. The crystal structures of new forms of silicon and germanium. *Acta Crystallogr* **17**, 752 (1964).
59. Crain, J. et al. Reversible pressure-induced structural transitions between metastable phases of silicon. *Phys. Rev. B* **50**, 13043–13046 (1994).
60. Birch, F. Finite Elastic Strain of Cubic Crystals. *Phys. Rev.* **71**, 809–824 (1947).
61. Klotz, S., Chervin, J., Munsch, P. & Le Marchand, G. Hydrostatic limits of 11 pressure transmitting media. *J. Phys. D: Appl. Phys.* **42**, 075413 (2009).
62. Mao, H.-K. & Bell, P. M. High-pressure physics: the 1-megabar mark on the ruby R1 static pressure scale. *Science* **191**, 851–852 (1976).

Acknowledgements

Support from NSF (CMMI-1943710 and DMR-2246991), ARO (W911NF2420145), and Iowa State University (Vance Coffman Faculty Chair Professorship and Murray Harpole Chair in Engineering) is greatly appreciated. This work is performed at HPCAT (Sector 16), Advanced Photon Source (APS), and Argonne National Laboratory. HPCAT operations are supported by DOE-NNSA's Office of Experimental Science. The Advanced Photon Source is a U.S. Department of Energy (DOE) Office of Science User Facility operated for the DOE Office of Science by Argonne National Laboratory under Contract No. DE-AC02-06CH11357. We also acknowledge CDAC-UIC for helping with the laser drilling of gaskets.

Author contributions

S.Y. and F.L. performed experiments. S.Y. collected and analyzed the data. V.I.L. conceived the study, supervised the project, analyzed the results, and developed theoretical models. K.K.P. and J.S. assisted with experiments. V.I.L. and S.Y. prepared the manuscript.

Competing interests

The authors declare no competing interests.

Additional information

Supplementary information The online version contains supplementary material available at https://doi.org/10.1038/s41467-024-51469-5.

Correspondence and requests for materials should be addressed to Sorb Yesudhas or Valery I. Levitas.

Peer review information *Nature Communications* thanks the anonymous reviewer(s) for their contribution to the peer review of this work. A peer review file is available.

Supplementary Information

Unusual plastic strain-induced phase transformation phenomena in silicon

Sorb Yesudhas[1]*, Valery I. Levitas[1,2,3*], Feng Lin[1], K. K. Pandey[4], and Jesse S. Smith[5]

[1]Department of Aerospace Engineering, Iowa State University, Ames, Iowa 50011, USA

[2]Department of Mechanical Engineering, Iowa State University, Ames, Iowa 50011, USA

[3]Ames National Laboratory, Iowa State University, Ames, Iowa 50011, USA

[4]High Pressure & Synchrotron Radiation Physics Division, Bhabha Atomic Research Centre, Mumbai 400085, India

[5]HPCAT, X-ray Science Division, Argonne National Laboratory, Argonne, Illinois 60439, USA

*Corresponding authors. Email: sorbya@iastate.edu, vlevitas@iastate.edu

This PDF file includes:

Supplementary Discussion 1. A new sequence of plastic strain-induced phase transformations in 100 nm Si

The plastic strain-induced PT studies have been carried out on 100 nm Si with Cu and S. S. gaskets of different thicknesses (Supplementary Table 1). The XRD patterns of strain-induced PTs study using a Cu gasket with 150-micron thickness inside RDAC are shown in Figs. 6a-b, 7c, d, Supplementary Fig. 7. A Cu gasket was pre-indented to 150 μm thickness using smooth diamonds with a culet size of 400 μm, and a 250 μm hole diameter was made using HPCAT, APS laser drilling machine. The sample was well-packed inside the sample chamber; no pressure calibrant or PTM was used. The XRD patterns were collected along the culet diameter with a 10-micron step size. The pressure distribution along the sample radius is maximum at the sample center. The appearance of a new peak at 2θ = 10.36° confirms the initiation of the Si-II phase at the sample center (Fig. 6b). The Si-I→Si-II phase transformation is initiated at 1 GPa at the sample center with a phase fraction of Si-II, 1.4% (Fig. 6a and Supplementary Table 2). The PT initiation pressure in Si-II is much smaller away from the sample center due to the larger plastic strain. Si-II PT initiation is observed at 0.3 GPa at r = 60 μm (1.1 GPa at r = 0) (Fig. 7d) and also at r = 70 μm, shear, ω = 5° (3.4 GPa at r = 0 and shear, ω = 0°) (Fig. 6b). The Si-I and Si-II phases coexist at 1 GPa. At 3.4 GPa, another peak appears to the right of the high intense (111) peak of the Si-I, identified as Si-III. The initiation of the Si-III phase is noticed at 0.6 GPa at r = 60 μm and shear ω = 10° (Fig. 7c). The Si-II and Si-III phases evolve with pressure; correspondingly, the phase fraction of the Si-I decreases. The Si-I, Si-II, and Si-III phases coexist at 3.4 GPa. Shear is applied at 3.4 GPa by the anvil rotation to various degrees at one rotation/hour. The phase fractions of Si-II and Si-III phases increase with pressure (Supplementary Table 2). The calculated averaged pressure is 5.1 GPa at r = 0 μm, ω = 149° (3.4 GPa at r = 0 μm, ω = 0°). The sample is pressurized to 6.1 GPa, and the shear is applied again (Fig. 6a and Supplementary Table 2). The Si-XI phase is observed at 10.2 GPa at r = 0 μm and ω = 82°, and all the four phases coexist, viz., Si-I, Si-II, Si-III, and Si-XI. With further compression, at 12.7 GPa, Si-I and Si-III phases disappear, and Si-II and Si-XI coexist (Fig. 6a and Supplementary Table 2). A maximum Si-II (54 %) is observed with a shear ω = 82° applied at 6.1 GPa. The average pressure of the sample at r = 0 μm and ω = 82° is 10.2 GPa (Supplementary Tables 2, 5). A maximum of 38.8 % Si-II is obtained at relatively low pressure (7.4 GPa) and shear ω = 5° at r = 10 μm (Fig. 9b). The coexistence of Si-I, II, III, and XI phases observed at 11.6 GPa and r = 0 μm (Fig. 9a). During loading, the Si-III phase

intermediate between Si-II and Si-XI is observed for the first time. Si-II and Si-III phases are initiated simultaneously in some regions away from the sample center. Also, in a few regions, the Si-III phase initiates before Si-II. The appearance of the Si-III phase is reproduced in all our shear experiments with Cu and S. S. gaskets. Si-III phase has also been seen in a few regions away from the sample center during plastic compression of 100 nm Si inside a 153-micron thick Cu gasket. Without shear, the initiation of Si-III requires a large pressure of 6.7 GPa (Table 1 and Fig. 7a). The calculated phase fraction for the Si-III without shear is 1%, whereas a maximum of 6% phase fraction is observed with shear (Fig. 7a and Supplementary Table 2).

Supplementary Discussion 2. Pressure-, stress-, and plastic strain-induced phase transformations under high pressure

The fundamental difference between the pressure- and stress-induced PTs under hydrostatic and non-hydrostatic loading and plastic strain-induced PTs at high pressure was formulated in[1]. Pressure- and stress-induced phase transformations start at crystal defects that naturally exist in a material and at stresses below the yield limit. These defects (e.g., various dislocation structures or grain boundaries) produce stress concentrators and serve as nucleation sites for a PT. First, nucleation occurs at defects with the strongest stress concentration; pressure should then be increased to cause nucleation at defects with decreasing levels of generated stresses. Plastic strain-induced PTs occur through nucleation and limited growth at defects (dislocations and twins) produced during plastic straining. Since there is a permanent generation of new defects and stress concentrators, there is no need to increase pressure; PT can be run by increasing plastic strain. Also, new defects generated during plastic flow may produce a much stronger stress concentrator than preexisting defects, significantly reducing the external pressure required for PT. It was concluded in[1] that plastic strain-induced transformations require very different thermodynamic, kinetic, and experimental treatments than pressure- and stress-induced transformations.

Supplementary Discussion 3. Failure of classical thermodynamics to describe plastic strain-induced phase transformations

Macroscopic continuum thermodynamics for pressure- and stress-induced PTs fails to describe the drastic reduction in PT pressure by one to two orders of magnitude due to plastic

straining. Indeed, the simplified expression for the mechanical part of the thermodynamic force for the PT is $W = -p\varepsilon_0 + \tau\gamma$, where p and τ are the pressure and shear stress, $\varepsilon_0 < 0$ and γ are the volumetric and shear transformation strains. For Si-I→Si-II PT, transformation strain tensor has principal component, $\boldsymbol{\varepsilon}_t = \{-0.514; 0.243; 0.243\}$ with volumetric strain of -0.249[2] and $\gamma = 0.5(0.243 + 0.514) = 0.379$. The main problem is that the shear stress is limited by the macroscopic yield strength in shear τ_y. Then $W = (p + 1.52\,\tau_y)\ 0.249$. Then, the same driving force under hydrostatic pressure can be reached at a pressure lower by $p = 1.52\,\tau_y$. Since for von Mises plasticity condition $\tau_y = \sigma_y/\sqrt{3}$, where σ_y is the yield strength in compression, we obtain $W = (p + 0.88\,\sigma_y)\ 0.249$. While it is difficult to estimate the yield strength of Si-I because it depends on pressure, grain size, and plastic strain, and PT to Si-II may interfere, we take $\sigma_y = 7.47$ GPa (i.e., $\tau_y = 4.31$ GPa) fitted in[3] to reproduce sawing experiments by the FEM simulations. Hence, the pressure required for Si-I→Si-II PT can be reduced by Δp = 6.56 GPa. Since under hydrostatic conditions for 100 nm Si, the PT pressure is 16.2 GPa, shear stresses can reduce it to 9.64 GPa. This value is close to 8.3 GPa obtained under uniaxial compression with small plastic strain in[4], considering all indeterminacies in our analyses and that pressure in[4] is reported in Pt or Au foil rather than Si. Thus, this approach misses 9.34 GPa to describe the experimentally observed PT pressure of 0.3 GPa.

For PT from Si-I to Si-III, $\boldsymbol{\varepsilon}_t = \{-0.002; -0.136; 0.058\}$ with the volumetric strain of $\varepsilon_0 =$ -0.088[5] and $\gamma = 0.5(0.136 - 0.002) = 0.067$. Then $W = (p + 0.76\,\tau_y)\ 0.088 = (p + 0.440\,\sigma_y)\ 0.088$, and with the same $\sigma_y = 7.47$ GPa, we obtain Δp = 3.28 GPa. Since PT to Si-III does not occur under hydrostatic pressure at all, shear stress reduction of the PT pressure Δp =3.28 GPa qualitatively disagrees with obtained Si-III at 0.6 GPa.

There are two main reasons for the obtained discrepancy. First, PT initiation pressure at room temperature is determined by the barrierless nucleation criterion rather than the phase equilibrium criterion, for which pressure can be significantly higher. For homogeneous loading under the action of all six components of the stress tensor, this criterion for Si-I to Si-II PT is determined by the first principle simulations in[2]. Second, we must consider the strong stress concentration at the defects generated during plastic flow.

Supplementary Discussion 4. Dislocation pileup-based mechanism (DPBM) for strain-induced phase transformations

The problem simplifies because we have to describe a very strong reduction in the PT pressure by one to two orders of magnitude and tens of GPa[6,7]. The largest and only known stress concentration of such magnitude can be produced at the tip of the dislocation pileups. Indeed, all stress components (and, consequently, pressure) are proportional to the number of dislocations in a pileup, N. Since N = 10-100, local stresses could be huge and increased by growing plastic deformation at relatively low pressure, thus driving PTs. The important point is that the deviatoric (non-hydrostatic) stresses near the defect tip are not bounded by the engineering yield strength but rather by the ideal strength in shear for a defect-free lattice, which may differ by a factor of 10 to 100. Local stresses of such magnitude may result in the nucleation of the high-pressure phase at an applied pressure that is not only significantly lower than that under hydrostatic loading but also below the phase-equilibrium pressure. In addition, such highly deviatoric stress states with large stress magnitudes cannot be realized in bulk. Such unique stresses may lead to nucleation of stable or metastable phases that could not be attained in bulk under hydrostatic or quasi-hydrostatic conditions.

The details of an analytical theory are presented in[1] and amended in the main text by including observation of more advanced theoretical and numerical phase-field[8,9], molecular dynamics[10], and concurrent atomistic-continuum simulations[11] approaches that the grain size does not limit the length of dislocation pileup l because it is localized at the grain boundary as a superdislocation. Since a detailed presentation of the analytical theory is not the goal of this experimental paper, we use a qualitative correspondence of the increase in the stress concentration and the PT pressure without placing these stresses in the phase nucleation criterion, which can be performed like in[1]. The above-advanced approaches overcame the main limitations of the analytical model[1], namely, single dislocation pileup, luck of dislocation nucleation and motion in the transforming grains, assumptions of linear elasticity, singular stresses at the tip of the dislocation pileup, etc. Still, they show nucleation at a pileup of a dozen dislocations may occur at pressure by more than an order of magnitude or 15 GPa below that under hydrostatic conditions. Even more, the high-pressure phase does not localize near the tip of the pileup but propagates away, and in nanograined material can reach the opposite side of the grain and coalesce with other growing regions, producing a large volume fraction of the high-pressure phase at low-pressure in

bicrystal and polycrystal (Supplementary Figs. 1-4). At all steady interfaces, the phase equilibrium condition $W = \sigma_{ij}\varepsilon_{ji} \cong -p\varepsilon_0 + \tau\gamma = \Delta\psi_\theta$ is met, where σ_{ij} and ε_{ji} are the components of the stress and transformation strain tensors, there is a summation over the repeating indices from 1 to 3, and $\Delta\psi_\theta$ is the jump in the thermal part of the free energy. While stresses reduce away from all tips of dislocation pile up, equilibrium is still possible due to the following reasons:

(a) Stresses/pressure required for phase equilibrium are significantly lower than for lattice instability required for barrierless nucleation.

(b) Severe plastic deformation reduces the grain size to the nanoscale and significantly increases the yield strength. Local shear stresses along the interfaces can be much higher than the resistance to the dislocation motion because of the lack of dislocation sources in the bulk of a nanograin and the necessity to nucleate for dislocations.

(c) Local stresses from dislocations generated during the deformation-PT process may stabilize interfaces. Large internal stresses at interfaces may remain after fully releasing external stresses.

(d) Generation by plastic straining of point defects, stacking faults, and disordering may arrest interfaces and keep metastable high-pressure phases at zero external stresses. Also, in the two-phase mixture, the high-pressure phase may still be under high internal pressure; for example, retaining at zero averaged pressure Si-II (c = 0.27, the rest is Si-III) is under the pressure in 3.6 GPa for the micron Si after non-hydrostatic compression with Cu gasket (Fig. 8a, Supplementary Table 11).

Let us estimate the possibility of phase equilibrium of a large volume of Si-II after its appearance at low pressure. The contribution of shear stress, $\tau = \tau_y = 4.31$ GPa to the transformation work was estimated above as equivalent to Δp = 6.56 GPa. The measured pressure in Si-II is 4-6 GPa higher than in Si-I at low pressure and small volume fractions of Si-II, and by 2-3 GPa at large volume fractions 38%. Combining these two numbers results in the total potential effective pressure increase by 8.56 to 9.86 GPa. Thus, an external pressure **of 0.4 to 1.44 GPa is** sufficient for nucleation and reaching an equilibrium pressure of ~10 GPa if large plastic shear is run under such constant pressure in RDAC (see Experimental results section).

Concerning PT to Si-III, which is not present in the phase diagram under hydrostatic loading, high pressure is not required. Since Si-III appears from Si-II during unloading, its phase equilibrium pressure with Si-I is lower than Si-II compared with Si-I. Pressure should be low but

with large plastic strains. Indeed, with increasing radius and plastic straining, the volume fraction of Si-III increases (Supplementary Table 2). Thus, the appearance of Si-III is nucleation controlled; it should be a proper combination of grain misorientation and orientation of a dislocation pileup with respect to the grain boundary and applied shear stress to cause nucleation of Si-III instead of Si-II, which should be observed.

Supplementary Discussion 5. Relevant results from the macroscopic modeling of sample behavior in DAC and RDAC

One of the concerns is that while Si-II and Si-III nucleate for strain-induced PTs at pressures much lower than that under hydrostatic conditions, Si-I completely disappears at high pressure comparable to that under hydrostatic conditions for micron Si. Retaining of Si-I up to 14.0 GPa (1.7% at 14 GPa and << 1% at 15.1 GPa) for plastic compression of micron Si (*vs*. 15.3 GPa under hydrostatic conditions) (Table 1; all data below are for the sample center) is due to relatively small plastic strain with stainless steel gasket and its effect on PT. For 100 nm Si with copper gasket, Si-I is retained up to 13.3 GPa (2.5%) under plastic compression and up to 12. 7 GPa (<< 1%) with small torsion *vs.* 18.1 GPa under hydrostatic loading; and for 30 nm Si, it is 13.2 GPa (2.2%) under plastic compression *vs*. 23.2 GPa under hydrostatic conditions[12]. The main reason is that the macroscopic behavior of a sample compressed in a DAC. During plastic compression, pressure grows whether we need this or not for PT. Our macroscale finite element method (FEM) simulations of the sample behavior in[13] demonstrate the following. While in the kinetic model for hexagonal hBN to wurtzite wBN p_{ε}^{d} = 6.7 GPa, there is no reverse PT, and the PT can be run to completion at a pressure slightly higher than 6.7 GPa with very large plastic deformation during compression, this PT does not complete at the center even at 52 GPa due to fast pressure growth but small plastic deformations. A similar situation occurs in our experiments on Si, but even worse because there are multiple alternative PTs, including reverse PTs. At the same time, under torsion in RDAC, plastic strain can be increased without limit with a much smaller pressure increase or, in specifically designed experiments, even at constant pressure. Supplementary Figs. 10 and 11 with FEM simulations show that, during torsion, much lower pressure is required to reach the same volume fraction of a high-pressure phase. However, since we performed only five exploratory torsion experiments on 100 nm Si with different goals, the geometric parameters of the gasket/sample were not optimized, and pressure increased during torsion. This could be avoided, but this is a topic for a separate, quite sophisticated work. Since

multiple PTs occur, we still need to determine the deformational and transformational properties of phases. PT pressure could be significantly reduced with the proper design of the experiment in RDAC. Note that in industrial applications (e.g., for the synthesis of superhard materials), reduction in the required pressure by fractions of a GPa is of great importance because it increases the number of working cycles that high-pressure device, cylinder and piston[14], can withstand before fracturing. Cost of the cylinder and piston is one of the major parts of the diamond cost. Thus, even current results for the disappearance of Si-I are of importance if this is required for applied purposes.

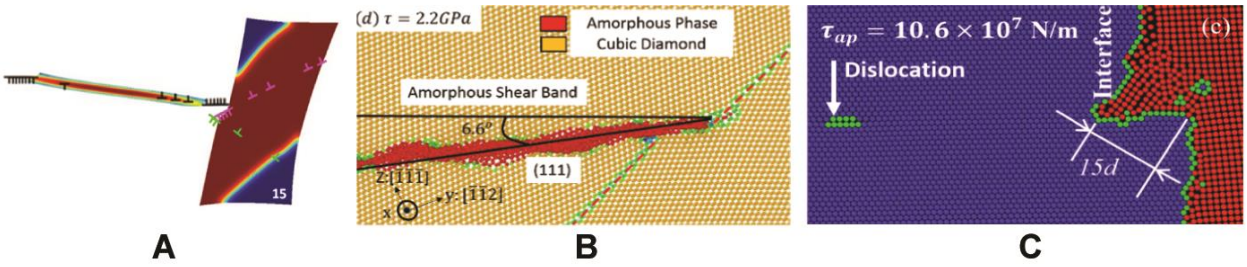

Supplementary Fig. 1. Dislocation pileups produce a step at the grain boundary that causes a phase transformation. (a) Dislocation pileup in the left grain produces a step at the grain boundary and cubic to tetragonal PT and dislocation slip in the right grain. The right grain is transformed by 77% at the applied pressure of 1.59 GPa, p_{ε}^{d} = 0 GPa, p_{h}^{d} = 15.9 GPa, p_e = 3 GPa and γ = 0.35. The nanoscale phase-field approach results from[9]. **(b)** Dislocation pileup in the right grain produces a step at the grain boundary in Si-I and amorphization in the left grain. Molecular dynamics results in from[10]. **(c)** Step at the phase interface boundary consisting of 15 dislocations, causing cubic to hexagonal PT. The atomistic portion of the concurrent continuum-atomistic approach from[11]. Reproduced with copyright permission 2024 from American Physical Society[9] (License Number: RNP/24/JUL/080873) and for Elsevier[10,11] (License Numbers: 5820380761218 and 5820400539939).

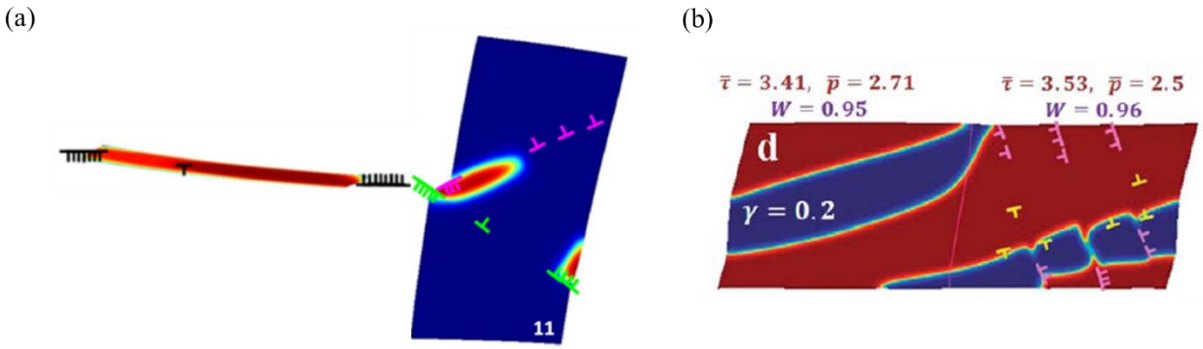

Supplementary Fig. 2. Dislocation-induced cubic to tetragonal phase transformation in bicrystal under compression and shear. (a) Dislocation pileup in the left grain initiates PT and dislocation slip in the right grain at zero applied pressure p and shear γ = 0.3. Material with p_ε^d = 0 GPa, $p_h^d = 15.9$ GPa and p_e = 3 GPa is treated. The nanoscale phase-field approach results from[9]. **(b)** Steady dislocation and phase structure in a bicrystal under shear γ = 0.2 when rotations of grains were considered. Averaged over the left and right grains, shear stress $\bar{\tau}$ and pressure $\bar{p}$ are shown above the grains. Material with p_ε^d = 2.0 GPa, $p_h^d = 15.75$ GPa and p_e = 10 GPa are studied. The nanoscale phase-field approach results in from[8]. Reproduced with copyright permission 2024 from American Physical Society[9] (License Number: RNP/24/JUL/080873).

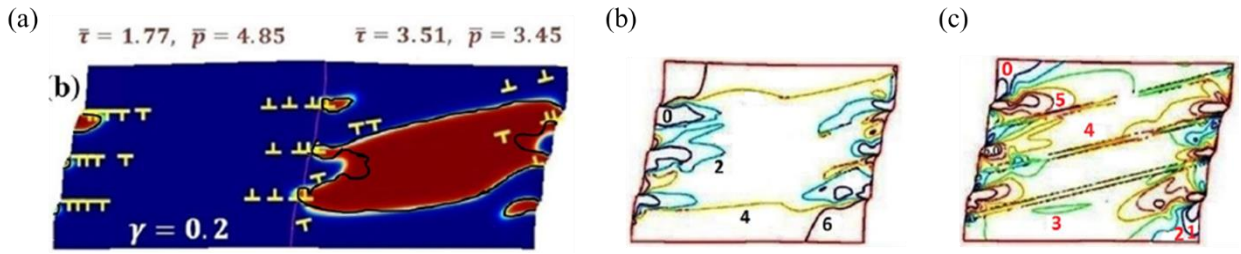

Supplementary Fig. 3. Dislocation-induced cubic to tetragonal phase transformation in bicrystal under compression p and shear τ. **(a)** Steady dislocation and phase structure in a bicrystal under compression and shear γ = 0.2. Averaged over the left and right grains, shear stress $\bar{\tau}$ and pressure $\bar{p}$ are shown above the grains. Black lines correspond to the fulfillment of the local phase transformation criterion $W = -p\varepsilon_0 + \tau\gamma = \Delta\psi_\theta$, demonstrating that major interfaces are in thermodynamic equilibrium. Material with p_ε^d = 2.0 GPa, $p_h^d = 15.75$ GPa and p_e = 10 GPa are studied. The practical luck of phase transformation in the left grain is because the crystal is perfectly aligned for dislocation slip, which releases shear stress. **(b)** and **(c)** are the pressure and shear stress level lines. Reproduced with copyright permission 2024 from Springer Nature[15] (License Number: 5820401496485).

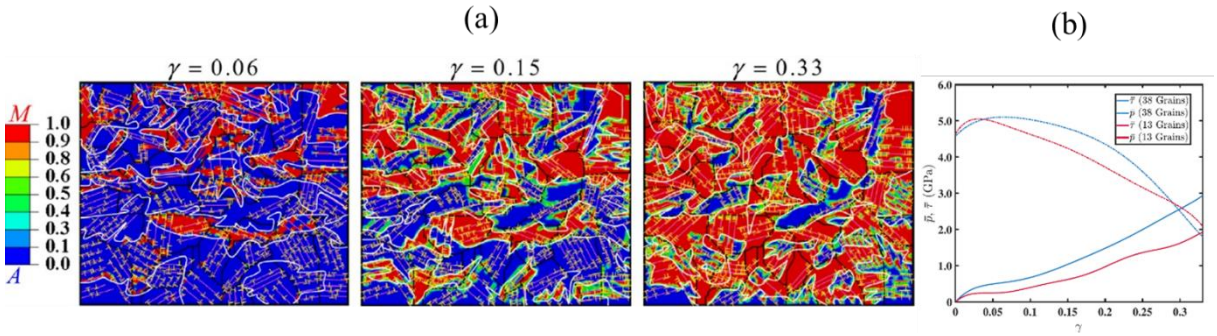

Supplementary Fig. 4. Dislocation-induced cubic to tetragonal phase transformation in polycrystal under compression and shear. (a) Dislocation and phase structure in a polycrystal with 38 grains under compression and shear and growing shear showing at the top of each panel. White lines correspond to the fulfillment of local phase transformation criterion, $W = -p\varepsilon_0 + \tau\gamma = \Delta\psi_\theta$, demonstrating that major interfaces are in thermodynamic equilibrium. Material with p_ε^d=2.0 GPa, $p_h^d = 14.70\ GPa$, and p_e = 10 GPa is studied. **(b)** Evolutions of the averaged pressure and shear stress for aggregates with 13 and 38 grains as a function of shear strain γ. Phase transformation starts at 5 GPa and small shear stress, after which pressure reduces, and shear stress grows during shearing. The scale-free phase-field approach results in from[16.17]. Reproduced with copyright permission 2024 from Elsevier[17] (License Number: 5820391387505).

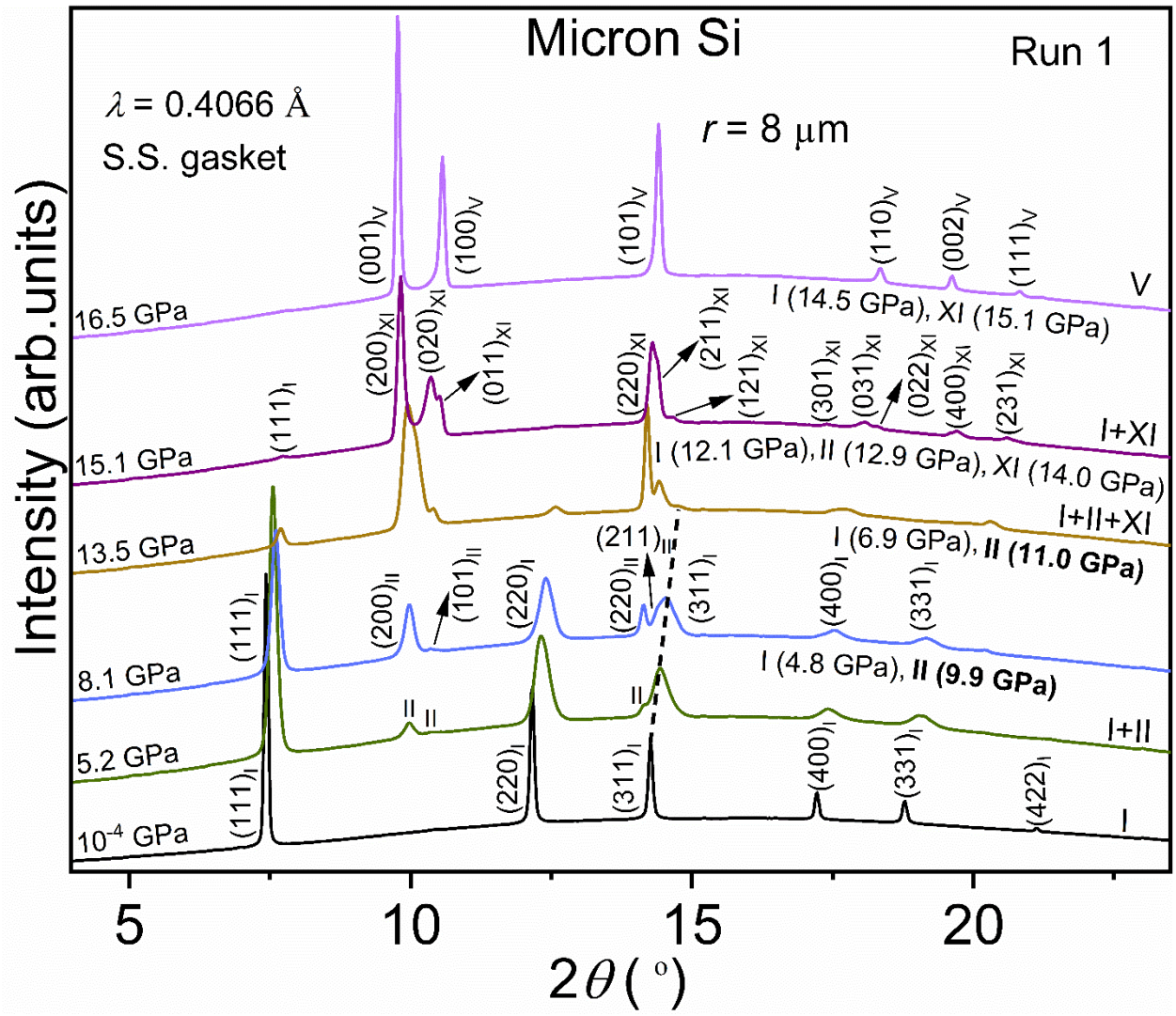

Supplementary Fig. 5. Indexing of Si-I, Si-II, Si-XI, and Si-V phases of micron size Si. XRD patterns of 100 nm Si for selected pressures under non-hydrostatic compression at r = 8 μm. The evolution of the (311) peak of Si-I is shown as a dashed line. The phase coexistence at various pressures is shown. The average pressure is shown on the leftmost side, and the pressure in each phase is shown on the right side, like in all other figures. The large pressure values of the Si-II compared to that of Si-I are shown in bold symbols.

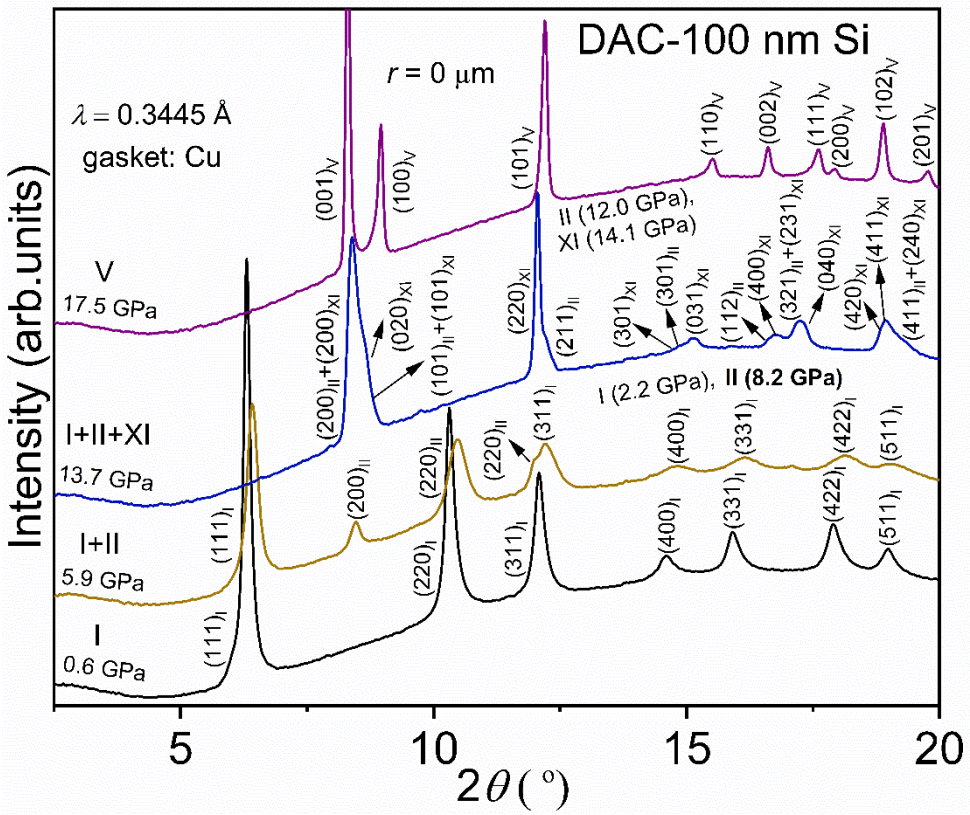

Supplementary Fig. 6. Indexing of Si-I, Si-II, Si-XI, and Si-V phases of 100 nm Si. XRD patterns of 100 nm Si for selected pressures under non-hydrostatic compression at r = 0 μm. The phase coexistence and average pressures are shown on the leftmost side.

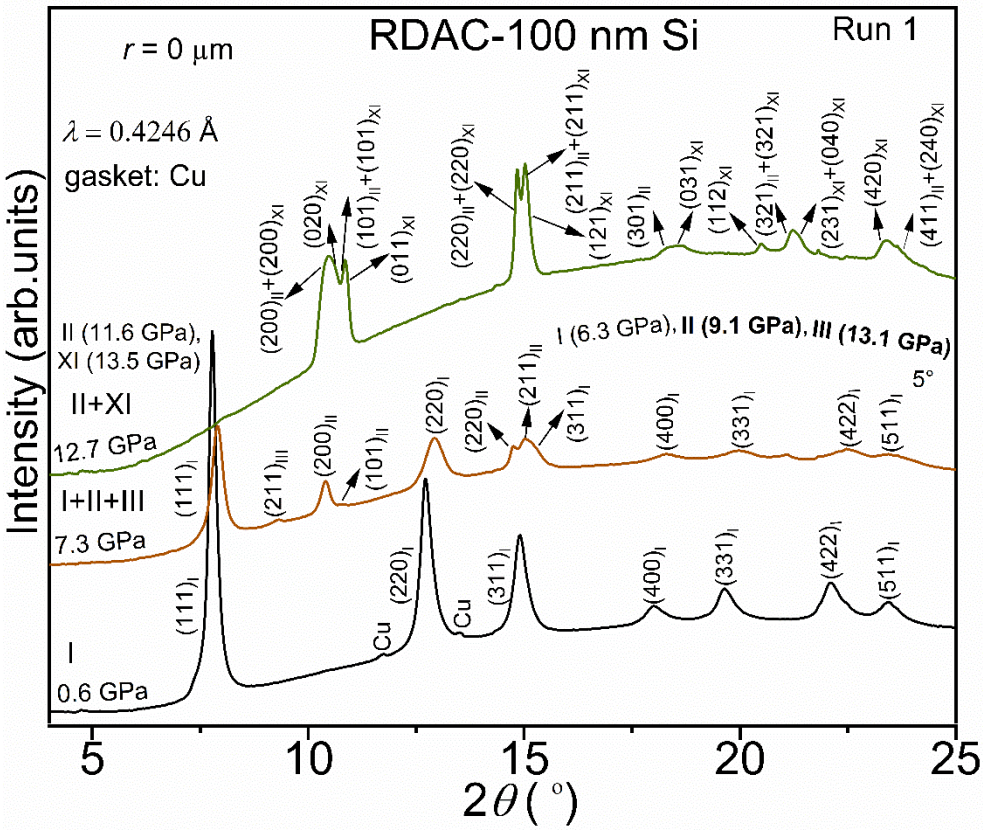

Supplementary Fig. 7. Indexing of Si-I, Si-II, Si-III, Si-XI, and Si-V phases of 100 nm Si under compression and shear inside RDAC (Run 1). XRD patterns of 100 nm Si at r = 0 μm for selected pressures.

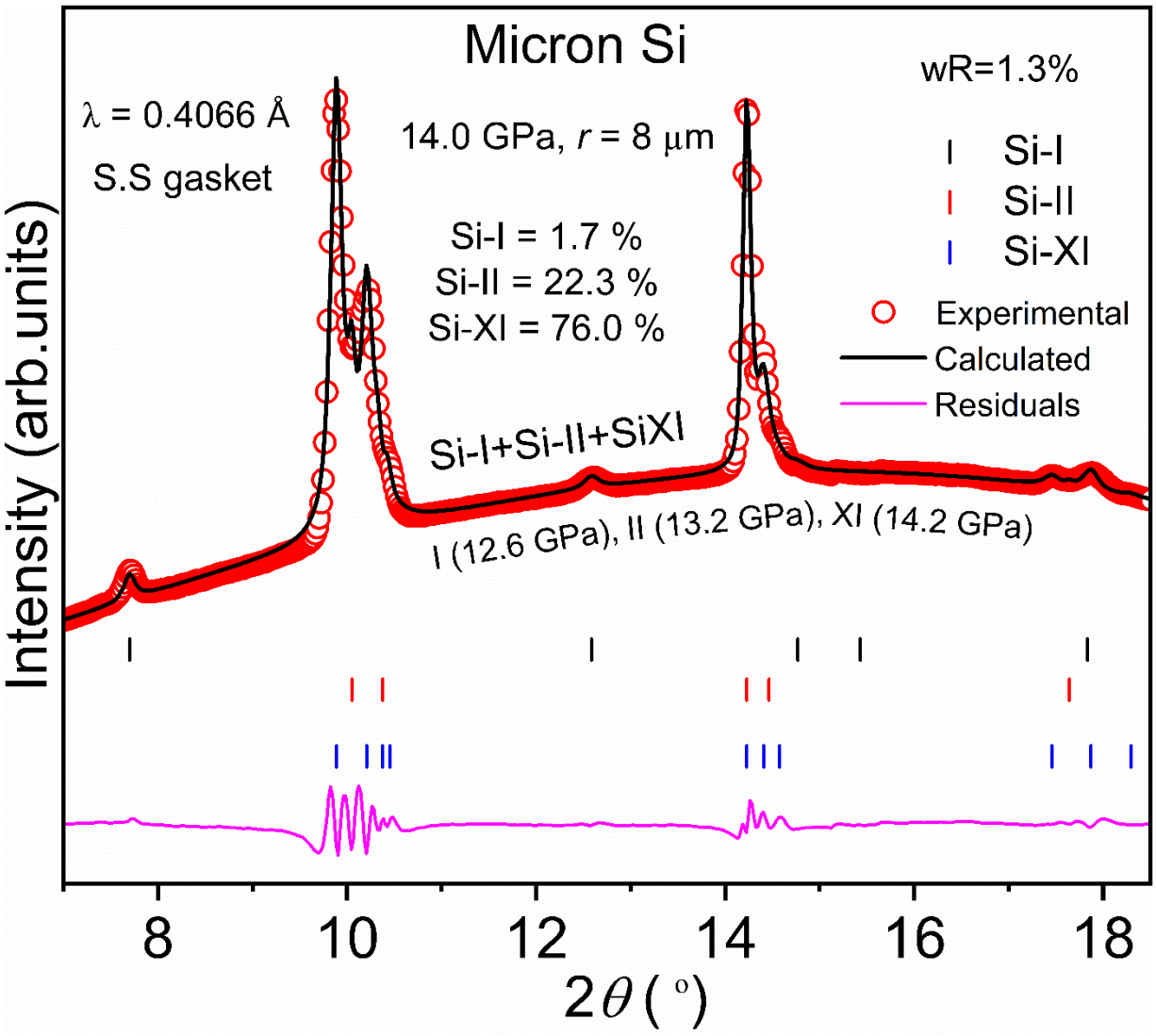

Supplementary Fig. 8. Coexistence of Si-I, Si-II, and Si-XI phases in micron Si: Rietveld refinement of non-hydrostatic compression of XRD data of micron Si at 14 GPa and r = 8 μm. The sample was plastically compressed inside a DAC using a stainless-steel gasket. The phase fractions (in %) of Si-I, Si-II, and Si-XI phases are shown.

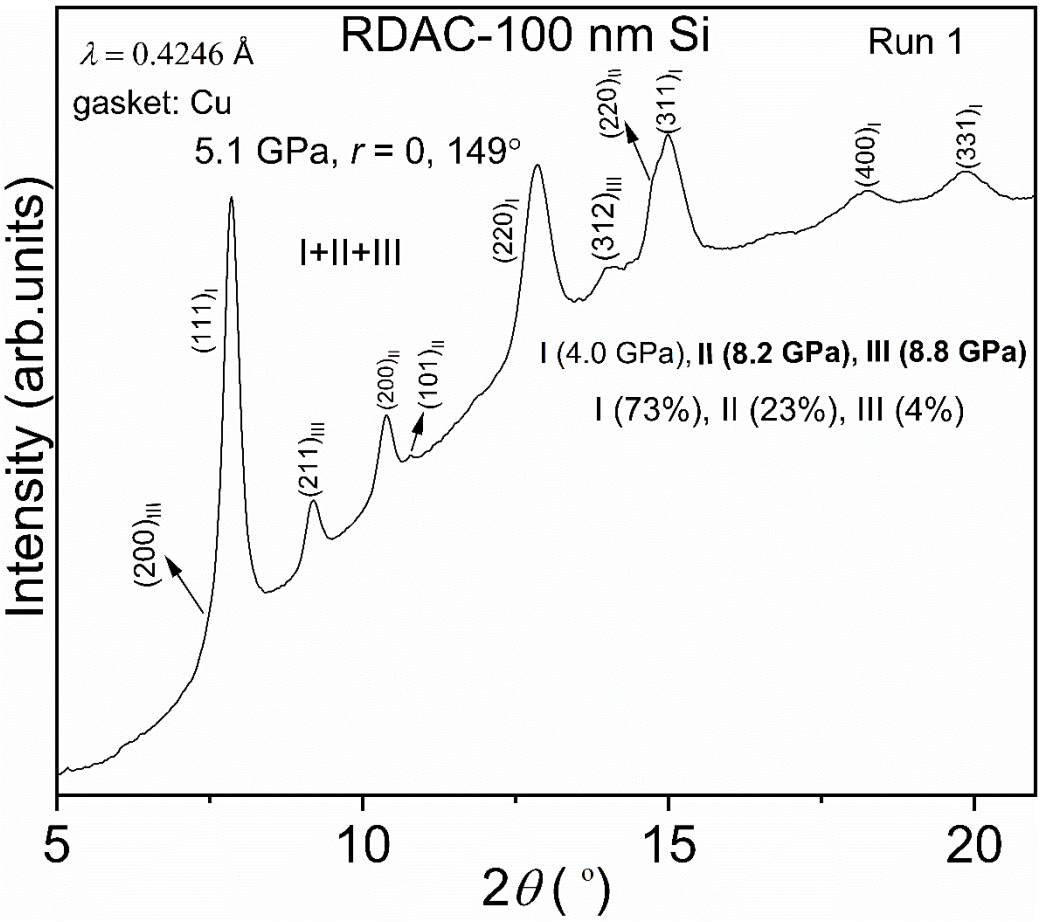

Supplementary Fig. 9. Indexing of Si-I, Si-II, and Si-III phases of 100 nm Si. Indexing of Si-I, Si-II, and Si-III phases of 100 nm Si at 5.1 GPa with shear, 149° and r = 0 μm.

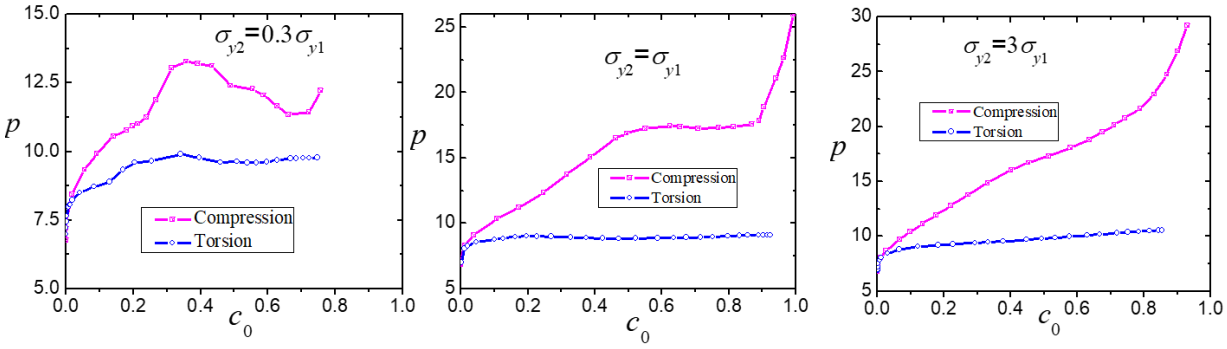

Supplementary Fig. 10. Variations of maximum pressure p in the sample versus the concentration of the high-pressure phase c_0 averaged over the entire sample for compression without torsion and torsion under a fixed axial force for three ratios of the yield strength of the high-pressure phase to the low-pressure phase σ_{y2}/σ_{y1}. Reproduced with copyright permission 2024 from AIP Publishing[18] (License Number: 5820420933340).

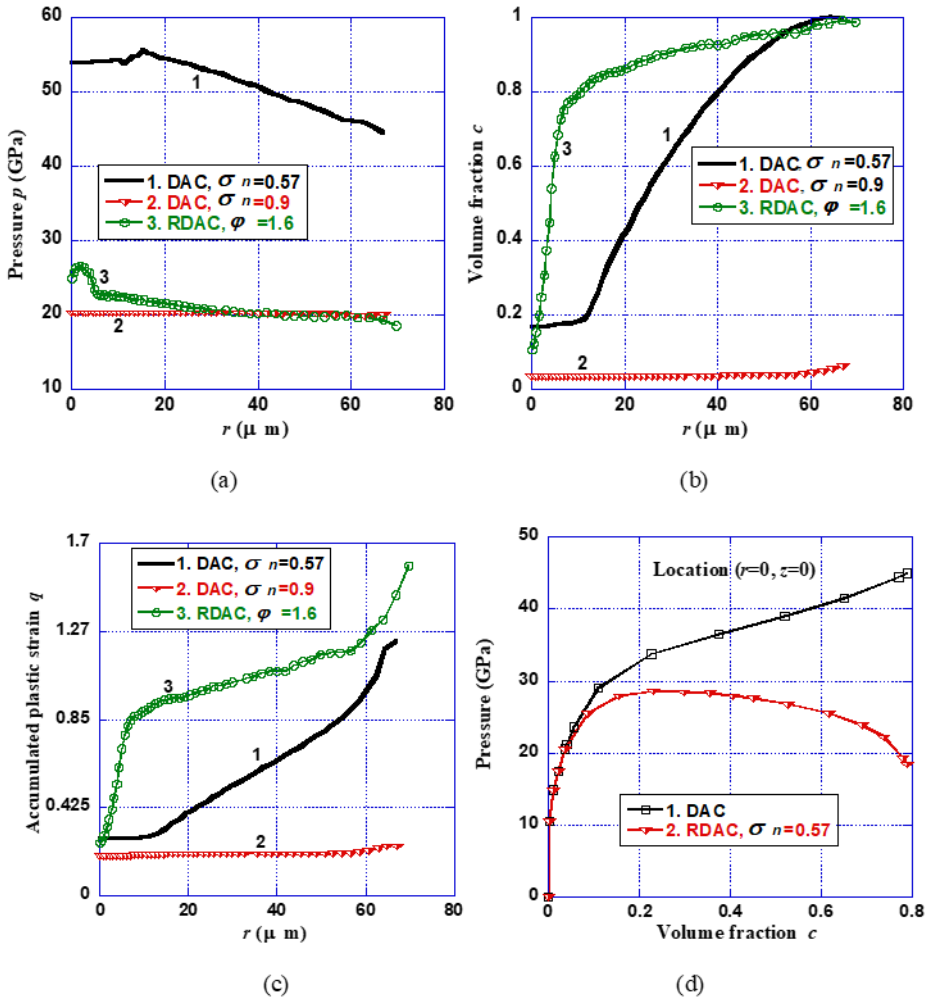

Supplementary Fig. 11. Variations of the pressure *p* (a), the volume fraction of the high-pressure phase *c* (b), and the accumulated plastic strain *q* (c) at the contact surface. Curves 1 and 2 are the results for DAC under the applied stress to the back side of the anvil of $\boldsymbol{\sigma}_n$= 0.9 and 0.57 GPa, respectively, and curve three stands for RDAC under $\boldsymbol{\sigma}_n$= 0.57 GPa and φ = 1.6. (d) The pressure *vs.* volume fraction of wBN *c* at the center of the sample in DAC and RDAC at $\boldsymbol{\sigma}_n$= 0.57 GPa. Reproduced with copyright permission 2024 from Elsevier[19] (License Number: 5820430258054).

Si particle size	Experiment name	Gasket type	Gasket hole diameter (μm), thickness (μm)	Compression/shear, DAC/RDAC	Diamond anvil, Culet size (μm)
Micron	Micron Si (Run 1) Micron Si (Run 2)	S. S. Cu	150, 120 150, 150	Compression, DAC Compression, DAC	Smooth, 300 Smooth, 400
100 nm	DAC-100 nm Si	Cu	220, 153	Plastic, DAC	Smooth, 400
100 nm	RDAC-100 nm Si (Run 1) RDAC-100 nm Si (Run 2) RDAC-100 nm Si (Run 3)	Cu S. S. S. S.	250, 150 120, 78 130,70	Shear, RDAC1 Shear, RDAC2 Shear, RDAC2	Smooth, 400 Rough, 230 Rough, 230
30 nm	30 nm Si	Cu	200, 134	Compression, DAC	Smooth, 400

Supplementary Table 1. Experimental details of various sample loading paths inside DAC/RDAC. S. S. is a stainless-steel gasket. Loadings are performed without PTM (non-hydrostatic compression). The details of RDAC1, RDAC2, and DAC are provided in "Methods". A description of sample loading paths for hydrostatic compression experiments is provided in[12]. Except for micron Si (Run 2), the PTs sequence for all other loading paths (compression and shear) is given in Table 1. Compact packing of the sample inside a thick, soft gasket was found to reduce the initiation pressure of Si-I→Si-II PT drastically. The initial thickness of the gasket used was in the range of 250 to 300 μm.

RDAC-100 nm Si (Run 1)									
Average pressure (GPa)	Si-I V (Å^3)	Si-II V (Å^3)	Si-III V (Å^3)	Si-XI V (Å^3)	Si-I Phase Fraction	Si-II Phase Fraction	Si-III Phase Fraction	Si-XI Phase Fraction	r (μm), p (GPa), Shear (°)
1E^{-4}	159.92(02)				1	0	0	0	
0.3	159.56(03)				1	0	0	0	0
0.6	159.10(07)				1	0	0	0	0
0.6	159.34(13)	57.7(9)	279.3(45)		0.973	0.020	0.007	0	60, 3.4, 10°
0.8	159.04(12)	57.51(30)			0.982	0.018	0	0	30
0.9	158.74(13)	57.43(31)			0.986	0.014	0	0	60
1.1	158.50(1)				1	0	0	0	0
1.0	158.82(13)	57.22(65)			0.986	0.014	0	0	0
1.6	158.26(13)	57.55(31)	270.3(42)		0.956	0.037	0.007	0	60, 3.4, 5°
1.9	157.59(15)	57.1(16)			0.984	0.016	0	0	0
3.4	155.94(13)	56.92(33)	272.7(40)		0.940	0.053	0.007	0	0, 3.4, 0°
7.3	152.22(12)	56.72(13)	266.3(22)		0.670	0.320	0.010	0	0, 3.4, 5°
6.4	153.53(13)	56.66(14)	267.3(17)		0.712	0.280	0.008	0	0, 3.4, 10°
5.8	154.24(18)	56.62(26)	268.8(13)		0.750	0.240	0.010	0	0, 3.4, 22°
4.9	155.15(15)	56.98(28)	272.22(69)		0.756	0.206	0.038	0	0, 3.4, 53°
5.1	154.92(15)	57.04(33)	273.7(11)		0.730	0.230	0.040	0	0, 3.4, 149°
5.0	155.11(15)	56.76(22)	271.22(79)		0.778	0.174	0.048	0	0
6.1	153.53(14)	56.76(30)	272.07(76)		0.770	0.177	0.053	0	0, 6.1, 0°
9.0	150.34(14)	56.46(11)	267.34(64)		0.565	0.377	0.058	0	0, 6.1, 15°
10.2	149.14(19)	56.34(06)	267.21(71)	56.00(03)	0.320	0.540	0.040	0.100	0, 6.1, 82°
11.6	147.29(24)	56.13(03)	264.6(15)	55.94(02)	0.092	0.512	0.009	0.387	0
12.7		55.87(02)		55.50(02)	0	0.457	0	0.543	0
12.9		55.82(03)		55.41(02)	0	0.416	0	0.584	0

Supplementary Table 2. Unit cell volume and phase fractions of Si-I, Si-II, Si-III, and Si-XI phases of 100 nm Si compressed and sheared inside an RDAC (run 1). The first column shows the actual pressure. The last column shows data for radial distance r of the point with respect to the sample center (r = 0), pressure p at the beginning of each torsion step, and rotation angle increment from the last compression without the torsion step. If just one number is shown in the last column, then it is radial distance r. The same designations are used for other Supplementary Tables. A relatively large phase fraction of Si-II is observed at reasonably low pressure (at 9 and 10.2 GPa). The sample is compressed up to 3.4 GPa; shear is created by continuously rotating one of the anvils up to 149°. Then, the sample is again compressed to 6.1 GPa and sheared to 82°.

RDAC-100 nm Si (Run 2)							
Average pressure (GPa)	Si-I V (Å^3)	Si-II V(Å^3)	Si-III V (Å^3)	Si-I Phase Fraction	Si-II Phase Fraction	Si-III Phase Fraction	r (μm), p (GPa), and Shear (°)
1E^{-4}	159.92(2)			1	0	0	
0.1	159.84(04)			1	0	0	0
0.3	159.60(05)			1	0	0	0
0.7	159.08(05)			1	0	0	0
0.8	158.87(09)			1	0	0	0
1.7	157.76(13)			1	0	0	0
2.2	157.05(15)	57.43(31)		0.990	0.010	0	0
3.3	155.80(16)	57.4(5)		0.982	0.018	0	30, 3.8, 1.8°
3.8	155.59(19)	56.96(20)		0.924	0.076	0	0, 3.8, 0°
5.0	154.29(15)	56.95(12)		0.871	0.129	0	0, 3.8, 0.6°
5.7	154.02(23)	56.77(38)	270.6(22)	0.790	0.188	0.022	60, 3.8, 46.2°
6.5	153.39(19)	56.84(14)	268.7(26)	0.656	0.329	0.015	50, 3.8, 45.6°
6.7	152.65(14)	56.93(09)		0.699	0.301	0	0, 3.8, 7.8°
7.1	152.50(15)	56.92(08)		0.585	0.415	0	0, 3.8, 15°
6.9	152.71(19)	56.93(11)	Initiated	0.606	0.394	0	0, 3.8, 29.4°
7.3	151.94(19)	56.88(14)	267.5(17)	0.535	0.429	0.036	0, 3.8, 43.8°
6.3	153.23(19)	57.37(28)	272.3(17)	0.561	0.394	0.045	0, 3.8, 58.2°
6.1	153.56(25)	57.39(25)	270.8(13)	0.563	0.424	0.013	0, 3.8, 72.6°
5.3	154.91(22)	57.43(44)	271.2(19)	0.616	0.359	0.025	0, 3.8, 87°
5.2	154.57(22)	57.58(32)	274.2(16)	0.624	0.349	0.027	0, 3.8, 101.3°

Supplementary Table 3. Unit cell volume and phase fractions of Si-I, Si-II, and Si-III phases of 100 nm Si compressed and sheared inside an RDAC (run 2). The sample is compressed up to 3.8 GPa; shear is created by continuously rotating one of the anvils at one rotation per hour at 3.8 GPa.

RDAC-100 nm Si (Run 3)					
Average pressure (GPa)	Si-I V (Å^3)	Si-II V (Å^3)	Si-I Phase Fraction	Si-II Phase Fraction	r (μm), p (GPa), and Shear (°)
1E^{-4}	159.92(2)		1	0	
0.1	159.80(04)		1	0	0
0.4	159.47(05)		1	0	0
0.7	158.98(07)		1	0	0, 0.7, 0°
0.8	158.96(07)		1	0	0, 0.7, 0.6°
2.6	156.58(18)		1	0	0, 0.7, 9.0°
5.9	152.96(17)	57.02(30)	0.890	0.110	10, 0.7, 15°
6.5	152.50(14)	56.86(12)	0.825	0.175	0, 0.7, 16.8°

Supplementary Table 4. Unit cell volume and phase fractions of Si-I and Si-II phases of 100 nm Si compressed and sheared inside an RDAC (run 3). The sample is compressed up to 0.7 GPa; shear is created by continuously rotating one of the anvils at one rotation per hour at 0.7 GPa.

RDAC-100 nm Si (Run 1)		
Average pressure (GPa)	Pressure in I, II, III, and XI phases, *p* (GPa)	*r* (μm), *p* (GPa), and Shear (°)
0.3	I (0.3)	0
0.6	I (0.6)	0
0.6	I (0.5), **II (6.3), III (5.8)**	60, 3.4, 10°
0.8	I (0.7), **II (6.9)**	30
0.9	I (0.8), **II (7.1)**	60
1.1	I (1.1)	0
1.0	I (0.9), **II (7.6)**	0
1.6	I (1.3), **II (6.7), III (10.7)**	60, 3.4, 5°
1.9	I (1.8), **II (7.8)**	0
3.4	I (3.1), **II (8.5), III (9.3)**	3.4, 0°
7.3	I (6.3), **II (9.1), III (13.1)**	3.4, 5°
6.4	I (5.2), **II (9.2), III (12.5)**	3.4, 10°
5.8	I (4.6), **II (9.3), III (11.6)**	3.4, 22°
4.9	I (3.8), **II (8.3), III (9.6)**	3.4, 53°
5.1	I (4.0), **II (8.2), III (8.8)**	3.4, 149°
5.0	I (3.8), **II (8.9), III (10.2)**	0
6.1	I (5.2), **II (9.0), III (9.7)**	6.1, 0°
9.0	I (8.1), II (9.8), III (12.5)	6.1, 15°
10.2	I (9.2), II (10.2), III (12.6), XI (13.3)	6.1, 82°
11.6	I (11.1), II (10.8), III (14.2), XI (12.6)	0
12.7	II (11.6), XI (13.5)	0
12.9	II (11.8), XI (13.7)	0

Supplementary Table 5. Average pressure and pressure in Si-I, Si-II, and Si-XI phases in 100 nm Si compressed and sheared inside an RDAC (run 1). Bold symbols show much larger pressure in the high-pressure phases than in Si-I.

RDAC-100 nm Si (Run 2)		
Average pressure (GPa)	Pressure in I, II, and III phases, *p* (GPa)	*r* (μm), *p* (GPa), Shear (°)
0.1	I (0.1)	0
0.3	I (0.3)	0
0.7	I (0.7)	0
0.8	I (0.8)	0
1.7	I (1.7)	0
2.3	I (2.2), **II (7.1)**	0
3.3	I (3.2), **II (7.0)**	30, 3.8, 1.8°
3.8	I (3.4), **II (8.4)**	0, 3.8, 0°
5.0	I (4.5), **II (8.4)**	0, 3.8, 0.6°
5.7	I (4.8), **II (8.9), III (10.6)**	60, 3.8, 46.2°
6.5	I (5.3), **II (8.7), III (11.7)**	50, 3.8, 45.6°
6.7	I (6.0), **II (8.5)**	0, 3.8, 7.8°
7.1	I (6.1), **II (8.5)**	0, 3.8, 15°
6.9	I (5.9), **II (8.5)**	0, 3.8, 29.4°
7.3	I (6.6), II (8.6), **III (12.4)**	0, 3.8, 43.8°
6.3	I (5.4), II (7.2), **III (9.6)**	0, 3.8, 58.2°
6.1	I (5.1), II (7.2), **III (10.4)**	0, 3.8, 72.6°
5.3	I (4.0), II (7.1), **III (10.2)**	0, 3.8, 87°
5.2	I (4.3), II (6.6), **III (8.5)**	0, 3.8, 101.3°

Supplementary Table 6. Average pressure and pressure in Si-I and Si-II phases of 100 nm Si compressed and sheared inside an RDAC (run 2).

RDAC-100 nm Si (Run 3)		
Average pressure (GPa)	Pressure in phases I and II, *p* (GPa)	*r* (μm), *p* (GPa), Shear (°)
0.1	I (0.1)	0
0.4	I (0.4)	0
0.7	I (0.7)	0, 0.7, 0°
0.8	I (0.8)	0, 0.7, 0.6°
2.6	I (2.8)	0, 0.7, 9.0°
5.9	I (5.6), **II (8.2)**	10, 0.7, 15°
6.5	I (6.1), **II (8.7)**	0, 0.7, 16.3°

Supplementary Table 7. Average pressure and pressure in Si-I and Si-II phases of 100 nm Si compressed and sheared inside an RDAC (run 3).

RDAC-100 nm Si (Run 1)					
Average pressure (GPa)	Si-I (nm)	Si-II (nm)	Si-III (nm)	Si-XI (nm)	*p* (GPa), Shear (°)
0.3	22.6(2)				
0.6	19.9(3)				
1.1	18.8(4)				
1.9	18.3(5)				
3.4	16.4(3)	15.0(20)			3.4, 0°
7.3	15.8(3)	15.5(6)			3.4, 5°
6.4	16.0(3)	15.6(7)			3.4, 10°
5.8	16.8(3)	15.4(13)	24.3(3)		3.4, 22°
4.9	18.1(4)	15.1(12)	22.2(25)		3.4, 53°
5.1	17.2(4)	13.0(8)	21.9(24)		3.4, 149°
5.0	18.6(4)	15.5(13)	26.5(39)		
6.1	20.8(6)	15.3(15)	26.6(39)		6.1, 0°
10.2	21.5(7)	17.1(3)	31.1(49)		6.1, 82°
11.6	17.3(4)	22.9(4)	23.8(12)	32.5(12)	
12.7		18.5(5)		28.4(8)	
12.9		17.2(4)		27.4(7)	

Supplementary Table 8. The crystallite size of Si-I, Si-II, Si-III, and Si-XI phases of 100 nm Si compressed and sheared inside an RDAC (run 1). The crystallite sizes at $r = 0$ of all the data are extracted using the Rietveld refinement method with GSAS II software.

RDAC-100 nm Si (Run 2)				
Average pressure (GPa)	Si-I (nm)	Si-II (nm)	Si-III (nm)	*p* (GPa), Shear (°)
0.1	33.0(5)			
0.3	30.4(5)			
0.7	25.6(4)			
0.8	18.3(3)			
1.7	17.1(4)			
3.8	16.3(3)			3.8, 0°
5.0	16.7(4)	12.6(17)		3.8, 0.6°
6.7	15.7(3)	12.4(5)		3.8, 7.8°
7.1	15.6(3)	11.3(3)		3.8, 15°
6.9	15.1(4)	11.3(3)		3.8, 29.4°
7.3	11.9(2)	11.6(4)	14.0(23)	3.8, 43.8°
6.3	12.2(3)	10.9(4)	12.2(19)	3.8, 58.2°
5.3	12.03(3)	10.95(5)	12.2(22)	3.8, 87.0°
5.2	12.5(4)	12.9(9)	12.5(13)	3.8, 101.3°

Supplementary Table 9. The crystallite size of Si-I, Si-II, and Si-III phases at *r* = 0 μm of 100 nm Si compressed and sheared inside an RDAC (run 2).

RDAC-100 nm Si (Run 3)			
Average pressure (GPa)	Si-I (nm)	Si-II (nm)	*p* (GPa), Shear (°)
0.4	25.9(3)		
0.7	20.9(3)		0.7, 0°
0.8	17.8(12)		0.7, 0.6°
2.6	16.8(8)		0.7, 9.0°
6.5	16.3(4)	12.2(13)	0.7, 16.8°

Supplementary Table 10. The crystallite size of Si-I and Si-II phases at *r* = 0 μm of 100 nm Si compressed and sheared inside an RDAC (run 3).

Experiment	Phase fraction of Si-phases (%)	Residual pressure in Si-II (GPa)
DAC-Micron Si (run 2) (Cu gasket)	Si-II: 27 %; Si-III: 73 %	3.6
RDAC-100 nm Si (run 2) (Cu gasket)	Si-I: 64 %; Si-II: 9 % and Si-III: 27 %	5.1

Supplementary Table 11. Phase fraction of Si phases and residual pressure in Si-II phase of micron and 100 nm Si after pressure released to 10^{-4} GPa.

Particle size of Si	Ruby pressure (GPa)	Pressure in Si-I (GPa)	Pressure in Si-II (GPa)	Pressure in Si-XI (GPa)
Micron size	13.5	13.7	12.9	14.1
100 nm	16.2	16.1	13.4	16.3
30 nm	14.6	14.8	–	13.7

Supplementary Table 12. The pressure in each phase of Si during the initiation of PTs for the hydrostatic experiments with He PTM[12]. The pressure in Si-II and Si-XI is smaller than in Si-I due to volume reduction during phase transformation.

Particle size	Si-I	Si-II	Si-III	Si-XI	Si-V
Micron					
V_0 (Å^3)	160.14(3)	60.29(14)	292.36	62.89(3)	15.204(6)
B_0 (GPa)	94.1(14)	133.0(5)	117.0	98.0(3)	107.3(16)
B_o'	5.0(3)	3.66(14)	4.0	1.9(4)	3.79(17)
100 nm					
V_0 (Å^3)	159.96(5)	61.22	292.36	61.746	15.226(6)
B_0 (GPa)	118.0(2)	133(5)	117.0	138(3)	102.0(5)
B_o'	3.1(4)	3.66(14)	4.0	1.266	6.5(8)
30 nm					
V_0 (Å^3)	160.06(6)	60.29(14)	292.36	62.89(3)	15.204(4)
B_0 (GPa)	90.6(19)	133(5)	117.0	98.0(3)	98.0(2)
B_o'	5.3(4)	3.66(14)	4.0	1.9(4)	5.0(2)

Supplementary Table 13. Parameters of the third-order Birch-Murnaghan EOS (BM3 EOS) obtained in[12] and used here for determining pressures for the Si phases of micron, 100 nm, and 30 nm Si. Details can be found in[12] and in Materials and Experimental Methods. The micron and 30 nm exhibit identical pressure dependence[12]. Since there are no Si-III EOS available for 100 and 30 nm Si, we assume that Si-III EOS for micron Si can be used for 100 and 30 nm Si.

References

1. Levitas, V. I. High-pressure mechanochemistry: conceptual multiscale theory and interpretation of experiments. *Physical Review B* **70**, 184118 (2004).
2. Zarkevich, N. A., Chen, H., Levitas, V. I. & Johnson, D. D. Lattice instability during solid-solid structural transformations under a general applied stress tensor: Example of Si I→ Si II with metallization. *Physical Review Letters* **121**, 165701 (2018).
3. Wallburg, F., Kuna, M., Budnitzki, M. & Schoenfelder, S. A material removal coefficient for diamond wire sawing of silicon. *Wear*, **204400**, 504-505 (2022).
4. Zeng, Z. Q., Ge, M., Chen, B., Lou, H., Chen, X., Yan, J., Yang, W., Mao, H.-K., Yang, D., & Mao. W. L. Origin of plasticity in nanostructured silicon. *Physical Review Letters* **124**, 185701 (2020).
5. Malyushitskaya, Z. V. Mechanisms responsible for the strain-induced formation of metastable high-pressure Si, Ge, and GaSb phases with distorted tetrahedral coordination. *Inorganic Materials*, **35**, 425-430 (1999).
6. Gao, Y., Ma, Y., An, Q., Levitas, V., Zhang, Y., Feng, B., Chaudhuri, J. & Goddard, W. A. Shear driven formation of nano-diamonds at sub-gigapascals and 300 K. Carbon 146, 364-368 (2019).
7. Levitas, V. I. High-pressure phase transformations under severe plastic deformation by torsion in rotational anvils. *Materials Transactions* **60**, 1294-1301 (2019).
8. Levitas, V. I. & Javanbakht, M. Phase transformations in nanograin materials under high pressure and plastic shear: nanoscale mechanisms. *Nanoscale* **6**, 162-166 (2014).

9. Javanbakht, M. & Levitas, V. I. Phase field simulations of plastic strain-induced phase transformations under high pressure and large shear. *Physical Review B* **94**, 214104 (2016).
10. Chen, H., Levitas, V. I. & Xiong, L. Amorphization induced by 60° shuffle dislocation pileup against different grain boundaries in silicon bicrystal under shear. *Acta Materialia* **179**, 287-295 (2019).
11. Peng, Y., Ji, R., Phan, T., Capolungo, L., Levitas, V. I. & Xiong, L. Effect of a micro-scale dislocation pileup on the atomic-scale multi-variant phase transformation and twinning. *Computational Materials Science* **230**, 112508 (2023).
12. Yesudhas, S., Levitas, V. I., Lin, F., Pandey, K. K., & Somayazulu, M. Effect of particle size on the phase transformation behavior and equation of state of Si under hydrostatic loading. *arXiv:2402.15092*
13. Feng, B. & Levitas, V. I., Coupled Elastoplasticity and Strain-Induced Phase Transformation under High Pressure and Large Strains: Formulation and Application to BN Sample Compressed in a Diamond Anvil Cell. *International Journal of Plasticity,* **96**, 156-181 (2017).
14. Yesudhas, S., Bundy F. P. & DeVries, R. C. Diamond: High-Pressure Synthesis. *In book: Reference Module in Materials Science and Materials Engineering, Elsevier Inc.,* 1-8 (2016).
15. Javanbakht, M. & Levitas, V. I. Nanoscale mechanisms for high-pressure mechanochemistry: a phase field study, *J. Mater. Sci.* **53** 13343-13363 (2018).
16. Levitas, V. I., Esfahani, S. E. & Ghamarian, I. Scale-free modeling of coupled evolution of discrete dislocation bands and multivariant martensitic microstructure. *Phys. Rev. Lett.* **121** 205701 (2018).
17. Esfahani, S. E., Ghamarian, I. & Levitas, V. I. Strain-induced multivariant martensitic transformations: A scale-independent simulation of the interaction between localized shear bands and microstructure. *Acta Materialia* **196**, 430-443 (2020).
18. Feng, B. & Levitas V. I. Effects of the gasket on coupled plastic flow and strain-induced phase transformations under high pressure and large torsion in a rotational diamond anvil cell. *Journal of Applied Physics* **119**, 015902 (2016).
19. Feng, B., Levitas V. I. & Li, W. FEM modeling of plastic flow and strain-induced phase transformation in BN under high pressure and large shear in a rotational diamond anvil cell. *International Journal of Plasticity* **113**, 236-254 (2019).